

## ABSTRACT

Title of thesis: 3D MULTIMODAL IMAGE REGISTRATION:  
Application to Equine CT and PET Images.  
Regani Sai Deepika, Master of Science, 2017

Thesis directed by: Professor Rama Chellappa  
Department of Electrical and Computer Engineering

Positron Emission Tomography (PET) is being widely used in veterinary medicine in recent years. Although it was limited to small animals because of its classical design and the large amount of radionuclide doses required, PET imaging in horses became possible with the introduction of a portable PET scanner developed by Brain Biosciences Inc. It was observed that this new modality could capture abnormalities like lesions that Computed Tomography (CT), Magnetic Resonance Imaging (MRI) and other modalities could not. Since 2016, PET imaging in horses is being studied and analysed.

While PET provides functional information characterizing the activity of lesions, it is useful to combine information from other modalities like CT and match the structural information to develop an accurate spatial representation of the data. Since biochemical changes occur much earlier than structural changes, this helps detect lesions and tumours during the early stages. Multimodal image registration is used to achieve this goal. A series of steps are proposed to automate the process of registration of equine PET and CT images. Multimodal image registration

using landmark-based and intensity-based techniques are studied. It is observed that a few tissues are not imaged in the PET, which makes image segmentation, an important preprocessing step in the registration process. A study of the segmentation algorithms relevant to the field of medical imaging is presented. The performance of segmentation algorithms improved with the extent of manual interaction and intensity-based registration gave the smallest time complexity with reasonable accuracy.

3D DEFORMABLE MULTIMODAL IMAGE REGISTRATION:  
Application to Equine PET and CT Images

by

Regani Sai Deepika

Thesis submitted to the Faculty of the Graduate School of the  
University of Maryland, College Park in partial fulfillment  
of the requirements for the degree of  
Master of Science  
2017

Advisory Committee:

Professor Rama Chellappa, Chair/Advisor

David Beylin(Brain Biosciences, Inc.), Advisor

Professor Behtash Babadi

Professor Joseph F. JaJa

© Copyright by  
Regani Sai Deepika  
2017

## Acknowledgments

First of all, I would like to express my profound gratitude to my advisor **Professor Rama Chellappa** for his guidance and support. He was very flexible, friendly and supportive and gave the freedom to work on a topic of my interest, which I think is important to bring out the best in a person.

I would like to thank **David Beylin (Brain Biosciences Inc.)** for mentoring me throughout the duration of the thesis and helping me to bring out the thesis in the present form. I thank Pavel Stepanov for his guidance during the initial phase of my work in the company, which was really important and helpful. Thanks to my colleagues at Brain BioSciences who were very welcoming and friendly.

I express my gratitude to **UC Davis Veterinary medicine** for providing the datasets and **Dr. Mathieu Spriet** for all the resources used in the thesis.

I would like to thank Professor Behtash Babadi and Professor Joseph F. JaJa for readily agreeing to be my panel members and for their valuable time and suggestions.

My heartfelt thanks to my roommates Pallavi, Harika and Soumya for bearing with me while working on the thesis and making the stay at College Park feel like home. A special thanks goes to my friends here at College Park: Shankar, Koutilya, Neha, Goutham, Harsha, Navaneeth, Nagashree, Raghu, Dayal for making my course of graduate study enjoyable and memorable. A special mention to my friend, Dwith, who from initiating the idea of doing a thesis to successfully finishing it, was a great company and resource.

The most important people to acknowledge are my parents and sister without whom this work would be impossible. They were supportive and inspiring in whatever I pursue. Thanking them is just not enough, I am indebted to them forever.

Finally, thanks to the Department of Electrical and Computer Engineering at the University of Maryland, College Park, Bill Churma, Emily, Melanie and other office faculty for giving me this wonderful opportunity. Thanks to the International Student and Scholar Services and the advisors for making the transition to the United States very smooth and enjoyable.

## Table of Contents

List of Tables	vi
List of Figures	vii
1 Introduction and Motivation	1
1.1 Positron Emission Tomography(PET)	1
1.2 Computed Tomography (CT)	3
1.3 Equine PET and CT registration	4
1.4 The equine bone anatomy	5
1.5 Summary of thesis	5
2 Related work	7
2.1 Image Segmentation	7
2.2 CT and PET Image Registration	13
3 Image Segmentation in CT images	14
3.1 Importance of Image Segmentation	14
3.2 Histogram based thresholding	16
3.2.1 Graph-cut based method	18
3.2.2 Fast March Algorithm	22
3.3 Results and Discussion	23
4 Image Registration of Equine PET and CT Images	35
4.1 Registration using Fiducial Points	36
4.2 Registration using Mutual Information	45
4.3 Registration using Edge Information	49
4.3.1 Edge Detection in PET images	51
4.3.2 Edge Detection in CT images	53
4.4 Some Results	56
5 Automatic equine PET and CT image registration	61
6 Conclusions and Future Work	67

A The 3D PET-CT Image Registration GUI	68
Bibliography	72

## List of Tables

3.1	Dice similarity index for different algorithms . . . . .	30
3.2	True Negative Fraction for different segmentation algorithms . . . . .	31
3.3	False Negative Fraction for different segmentation algorithms . . . . .	32
3.4	True Positive Fraction for different segmentation algorithms . . . . .	33
3.5	False Positive Fraction for different segmentation algorithms . . . . .	34
4.1	Variation of Transformation Parameters with Noise . . . . .	41
4.2	Source, Target and transformed fiducial points . . . . .	43
4.3	Affine parameters for PET-CT using fiducial points . . . . .	43

## List of Figures

1.1	The Cerepet . . . . .	2
1.2	Classical and portable PET scanners . . . . .	3
1.3	PET and CT Registered . . . . .	4
1.4	Equine Forelimb Anatomy . . . . .	6
2.1	Typical Equine PET Image . . . . .	8
2.2	Partial Volume effect . . . . .	9
2.3	Typical Equine PET Image . . . . .	10
2.4	Typical Equine PET Image . . . . .	13
3.1	Registration by segmenting the hoof . . . . .	15
3.2	Variation in PET based on age . . . . .	15
3.3	CT Image before segmentation . . . . .	16
3.4	Histogram thresholding in CT Image . . . . .	17
3.5	Segmented CT image and the corresponding PET image . . . . .	18
3.6	CT Histograms . . . . .	19
3.7	Some results of Histogram-based Thresholding . . . . .	20
3.8	Graph-cut Method of Segmentation . . . . .	21
3.9	Fast-March Method of Segmentation . . . . .	23
3.10	Segmentation of CT (3D) . . . . .	24
3.11	Segmentation Results . . . . .	27
3.12	Segmentation Evaluation(Dice Coefficient) . . . . .	29
3.13	Segmentation Evaluation(Absolute Area Difference) . . . . .	29
4.1	Source and Target Points(2D) . . . . .	38
4.2	Transformed and target points(2D) . . . . .	39
4.3	Source and Target Points(3D) . . . . .	39
4.4	Transformed and Target Points(3D) . . . . .	40
4.5	PET and CT fiducial points . . . . .	42
4.6	Fiducial Points Correspondence . . . . .	42
4.7	Aligned PET and CT using Fiducial Points . . . . .	44
4.8	Mutual Information and the alignment accuracy . . . . .	46
4.9	Multiresolution Image Pyramid . . . . .	48

4.10	Direct Edge detection on PET image . . . . .	52
4.11	Edge detection on PET image . . . . .	53
4.12	Direct Edge Detection on CT . . . . .	54
4.13	Edge Detection in CT images . . . . .	54
4.14	Edge Image of PET and CT . . . . .	55
4.15	Edge Alignment using the Edge Metric . . . . .	56
4.16	Figure with caption indented . . . . .	57
4.17	Percentage of time taken for each step in coarse registration . . . . .	58
4.18	Similarity percentage in the coarse registration of PET-CT . . . . .	59
4.19	Time Complexity for Coarse Registration of PET-CT . . . . .	60
5.1	Flow chart of the registration process . . . . .	61
5.2	Sample DICOM header . . . . .	63
5.3	The PET and CT voxels . . . . .	64
5.4	Flipped dimensions in CT . . . . .	65
A.1	Axes in GUI . . . . .	69
A.2	Modules in the PET-CT GUI . . . . .	70
A.3	MIP Images of PET and CT in GUI . . . . .	71

## Chapter 1: Introduction and Motivation

### 1.1 Positron Emission Tomography(PET)

Positron (Positive electron) is a positively charged subatomic particle with the same mass and magnitude of charge as electron. It is an antiparticle of a negative electron, first discovered by a Nobel Prize winner, Carl David Anderson in 1932 [2]. Positrons quickly react with the electrons of ordinary matter by annihilation (conversion of a particle and antiparticle into energy) to produce gamma radiation, the shortest wavelength and highest energy radiation in the electromagnetic spectrum. Amongst other sources of positrons, the one that interests us are the positrons emitted from man-made radioactive sources which can be used in medical diagnosis in a technique known as positron emission tomography (PET). Tomography means a technique of displaying a cross-section of a body using penetrating waves like ultrasound or X-rays. PET uses radionuclides that decay by emission of positrons like carbon-11, nitrogen-13, oxygen-15 and fluorine-18.

The annihilation radiation emitted consists of two photons emitted simultaneously and travelling in opposite directions. This radiation can be detected by a pair of radiation detectors which localize the site of annihilation event to a straight line joining the two detectors as shown in Fig. 1.1. Among the emerging medical imag-

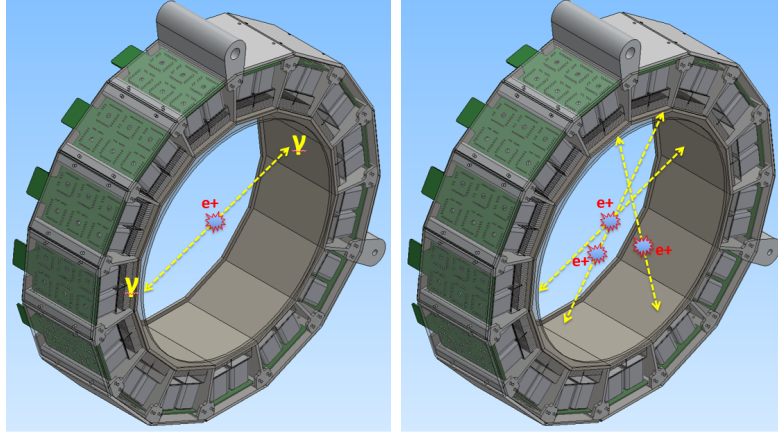


Figure 1.1: The Cerepet Scanner of Brain Biosciences Inc. The radiation detected by two opposite detectors enables localizing the annihilation event to a straight line.

ing modalities, PET belongs to the class of nuclear medicine. This is because the image forming variable is the distribution of a radionuclide which is administered using a radiopharmaceutical prior to the imaging procedure. [33].

Physiological and biochemical changes in an organ trigger each other. The objective of PET is to noninvasively study the biochemical changes in an organ that are significant to the organ studied. This helps in early discovery of changes in tissues, since changes in function often occur before changes in anatomy [10].

PET imaging in horses was not possible until recent past because of the classical design of the PET scanner and the large amounts of radioactive tracer required. A portable PET scanner was introduced by Brain Biosciences Inc, overcoming these difficulties. Fig. 1.2 shows a classical PET scanner and the one developed by Brain Biosciences Inc. The most commonly used tracer is FDG (fluorodeoxyglu-

cose) which is an analogue of glucose. The regional glucose intake depends on the tissue metabolic activity. It has been observed that the PET modality could detect lesions which went unnoticed using other modalities [31]. This motivates us to improve the techniques and analyse images obtained from the portable PET scanner.



Figure 1.2: (left) Classical PET scanner, (Right) A portable PET scanner

## 1.2 Computed Tomography (CT)

Computed Tomography makes use of X-rays to obtain the structure of an organ. As X-rays pass through an organ, they are absorbed to various extents by different tissues thus creating a matrix of X-ray beams of various strengths. This matrix is processed to obtain a CT image. CT images are particularly useful while imaging bone fractures, bone tumors or eroded joints. Although some lesions can be imaged

in a CT, they are difficult to identify because of the low contrast. PET image on the other hand, provides a very good contrast with the area surrounding the lesion. This is demonstrated in Fig. 1.3. This motivates us to study image registration of PET and CT images to combine information from the two modalities.

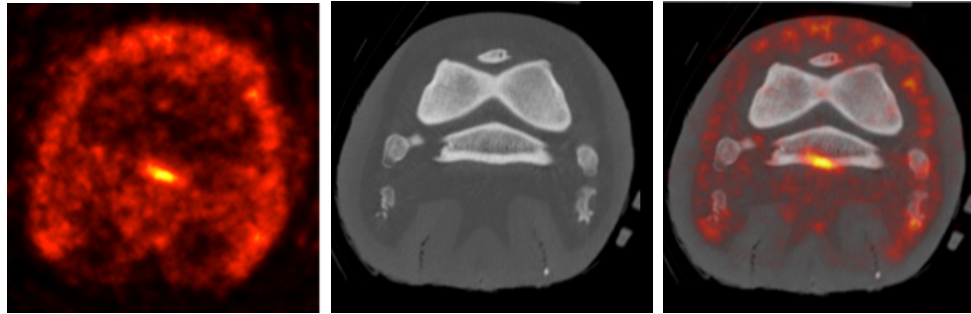


Figure 1.3: (left) A PET image showing Occult Navicular lesion in a horse, (middle) A CT image of the same organ, (Right) A registered image of PET and CT

### 1.3 Equine PET and CT registration

Image registration refers to matching features in different images to obtain a single image with common spatial coordinates. Image registration, in general, has varied applications like panorama creation, virtual/augmented reality, live streaming, surveillance and many more. This thesis discusses image registration by considering two types of tomographies discussed in section 1.1 and 1.2, the Positron Emission Tomography (PET) and the Computed Tomography (CT). While CT provides structural information, PET provides functional information. Having access

to both types of information helps to gain a better understanding of the subject. The multi-modal image registration algorithm can be used to obtain accurate spatial representation of data. Throughout the thesis, we will consider the coordinates of the PET image as the reference. Hence, our aim is to find a transformation to the CT image which will match the coordinates of the PET image. There are a plethora of techniques already proposed in the literature for image registration. Recent advancements in this area are minor variations to some of the existing algorithms for specific applications. We will design a sequence of steps required to automate/semi-automate the process of equine PET and CT registration. Challenges include difference in voxel sizes, difference in the regions imaged and computational complexity due to large image sizes.

## 1.4 The equine bone anatomy

Before going into further details of the equine PET and CT registration problem, we present here the equine bone anatomy. Fig. 1.4 shows the equine forelimb and rearlimb anatomy [6]. Most of our analysis and results will be on the foot, fetlock, tarsus and carpus.

## 1.5 Summary of thesis

In chapter 2, we present an overview of related works in image registration and image segmentation. In chapter 3, we discuss in detail, the importance of image segmentation, define our registration problem, implement some standard segmentation

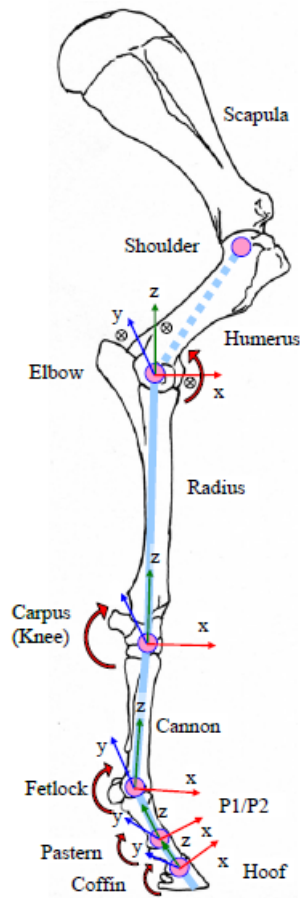


Figure 1.4: The Equine Forelimb anatomy

algorithms and evaluate the performance. In chapter 4, we perform registration using landmark-based and intensity-based methods. We also discuss a deformable registration problem specific to the equine anatomy. In chapter 5, we put together all the techniques to design a sequence of steps to automate/semi-automate the registration of equine PET and CT images. Finally, in chapter 6, we present some conclusions and possible future work.

## Chapter 2: Related work

### 2.1 Image Segmentation

Image Segmentation refers to dividing an image into regions which are more meaningful and easier to analyse. It is a well studied research topic and a huge topic on its own. We will bias our discussion to applications of image segmentation in the medical imaging domain. Image segmentation algorithms in medical imaging domain are required to delineate anatomical structures and other regions of interest. Fig. 3.2 shows an example of an MRI image of the brain, showing gray matter (blue), white matter (yellow), and cerebral spinal fluid (red). The general goal of any image segmentation algorithm is to automate the process of segmentation in order to be able to handle large amount of data as well as to achieve fast and accurate results. Image segmentation algorithms are specific to the application, image modality and the type of organ under study. Though some generic algorithms do exist, application specific algorithms are generally more faster and accurate because of the prior information.

Before diving into the study of image segmentation algorithms, we discuss some of the issues encountered in the performance of algorithms.

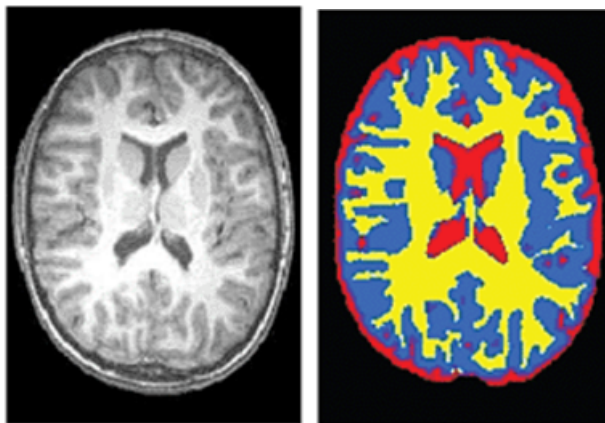


Figure 2.1: Example of an MRI image of the brain, showing gray matter (blue), white matter (yellow), and cerebral spinal fluid (red).

[21]

1. **Partial volume effect:** This occurs when more than one tissue contributes to the intensity of a voxel causing blurring of the image across boundaries. Soft segmentations allow a voxel to belong to different classes allowing for an uncertainty. Fig. 2.2 shows an example of partial volume effect. A number of techniques have been proposed to overcome the partial volume effect. ([34], [5], [38])
2. **Intensity inhomogeneity:** Intensity inhomogeneity refers to the variation of intensity of the same tissue across the image. This is particularly seen in MRI images due to image acquisition process. Different methods have been proposed to rectify intensity inhomogeneity, a review of such methods is presented in [37]
3. **Presence of artifacts:** Presence of noise can effect algorithms based on

edge information. Motion blurring is caused due to the motion of the subject during the image acquisition process. Different methods have been proposed for corrections, one method for the correction of motion blur in PET images can be found in [27] and an interesting method using blind deconvolution is presented in [29]

4. **Closeness in the gray level of different tissues:** Low contrast between the tissues makes it difficult for segmentation algorithms that depend on intensity values to identify regions of interest.
5. **Tradeoff between interaction and accuracy:** Even the "automated" image segmentation algorithms require some kind of manual interactions such as providing the initial conditions or a seed point. To look at extreme cases, manual segmentation is the most accurate and segmentation without any input is the most uncertain.

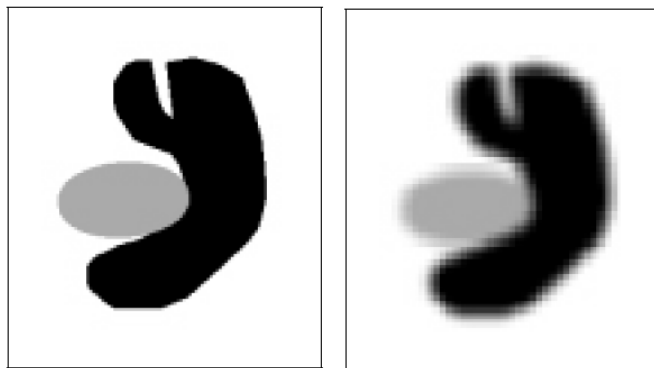


Figure 2.2: Partial volume effect.(Left) Ideal Image, (Right) Acquired Image [26].

Fig. 2.3 shows a broad taxonomy of image segmentation algorithms. We will present an overview of some of these algorithms here.

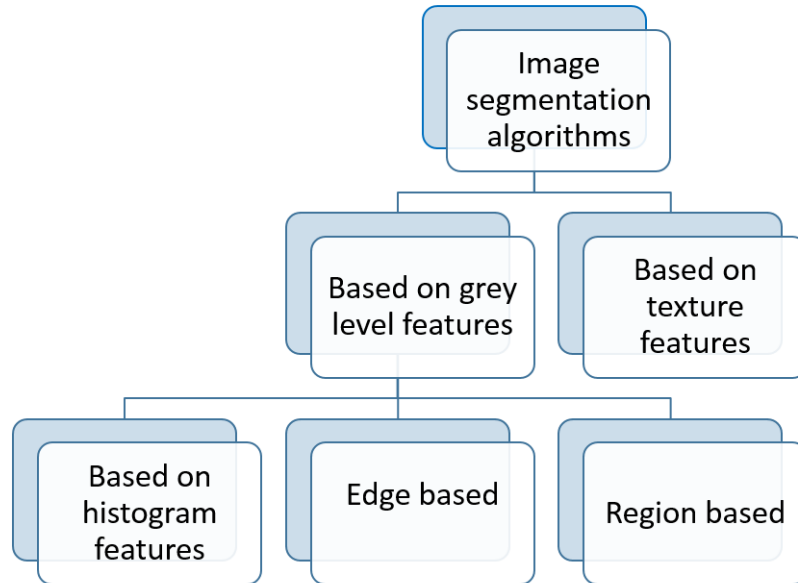


Figure 2.3: Classification of Image segmentation algorithms

1. **Histogram-based:** In this class of algorithms, segmentation is done using a histogram feature, which in most cases is the gray level intensity. We can either use a single threshold for bi-modal histogram or use multiple thresholds for multi-modal histogram. The threshold is applied as follows:

$$M(i, j) = \begin{cases} 1 & T_1 < p(i, j) \leq T_2 \\ 2 & T_2 < p(i, j) \leq T_3 \\ \dots & \dots \\ 0 & \textit{otherwise} \end{cases} \quad (2.1)$$

The main limitation of intensity-based threshold is that the performance is affected by the choice of threshold. Also, the approach does not take into consideration the spatial information and hence is affected by noise and intensity inhomogeneities. Selection of a proper threshold is difficult, automating the choice of the threshold is even bigger a challenge. Ostu's method tries to automate the selection of a threshold by trying to minimize the intra-class variance and set a global threshold assuming a bi-modal image. [24]

2. **Edge-based segmentation:** The main idea of the edge-based segmentation is to divide the image based on boundaries. The first step is to detect edges in the image using different edge detection operators like Prewitt, Sobel, Roberts(first derivative), Laplacian (second derivative), Canny and Marr-Hilclrath. Once the edges are detected, they need to be combined to form an edge chain to achieve segmentation. Fake and weak edges pose a challenge and can be removed by thresholding operations. The class of algorithms based on edge detection can further be subdivided into those that use edge relaxation [13], border detection [20], [19] and Hough transform. [18]. The main limitations of these methods is that they are affected by noise. Since

edge detection is essentially high pass filtering, we end up amplifying the high frequency noise. It is found that the edge-based methods used in conjunction with region-based methods provide very good results.

3. **Region-based methods** Region-based methods are based on the principle of homogeneity. Pixels/voxels with similar properties are clustered together to form homogeneous regions. A common property used is the gray level of the pixels [17]. Region-based segmentation algorithms can be further classified into those that use region merging, region splitting, region split and merge, watershed transformation, k-means clustering. The limitations of region-based methods are due to over-segmentation and under-segmentation. One way to overcome this is to combine it with edge-based approaches.
4. **Texture-based features** Texture-based segmentation algorithms subdivide the image into regions based on different texture properties. Some methods for extracting texture features are co-occurrence matrix method based on statistical description of gray levels of an image, gray level run length method, fractal texture description method, syntactic method and the Fourier filter method. [28]

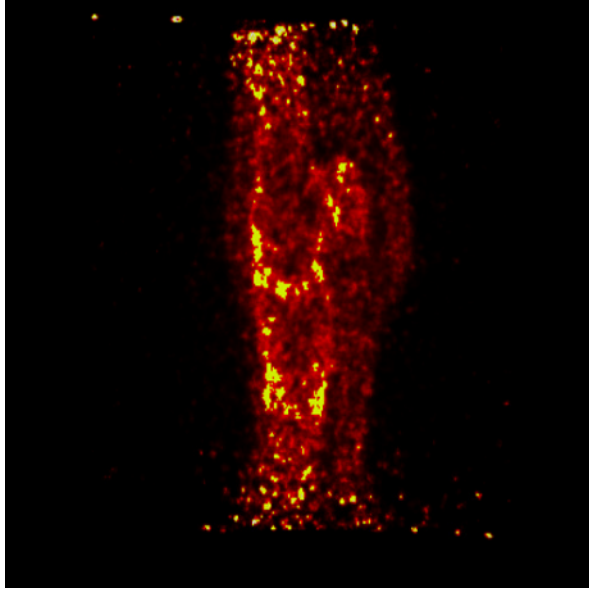


Figure 2.4: A typical Equine PET Image

## 2.2 CT and PET Image Registration

Integrating PET and CT in one image helps morphological and functional imaging characteristics to be studied at the same time. The registration also gives scope for improving the location accuracy of the detected lesions in the PET images. Rigid body deformation in combination with localized cubic B-splines can be used to capture small deformities in multimodal images. These deformities could correspond to movement in the subject during the image acquisition process or the chest movement, for example. It has been reported that the 3D PET-CT registration process takes approximately 100 minutes. [22]

## Chapter 3: Image Segmentation in CT images

### 3.1 Importance of Image Segmentation

PET images use a radioactive nuclide ( $^{18}F - FDG$ ) to record activity as discussed in section 2.1. Hence the coffin bone is not imaged using PET since the emission of positrons is not possible. Image segmentation is used in medical imaging to study anatomical structures, identify some regions of interest and applications such as measuring tissue volume to estimate the growth of a tumor. In the equine PET and CT registration problem, image segmentation is used to remove the hoof of the horse foot before registering with the PET image. One case of a PET and CT image registration problem which requires segmenting the hoof is shown in Fig. 3.1.

Depending on the age of the horse, the regions of activity vary as shown in Fig. 3.2. We would either choose to remove the coffin bone or both the coffin and pastern bones. This requirement is based on the portions imaged in PET so as to achieve better registration. Once we obtain the transformation, we can apply the transformation on the original image to get the registered PET and CT image.

We will apply histogram based thresholding, graph-cut and fast-march algorithms for image segmentation in CT images. These methods are explained in the next sections.

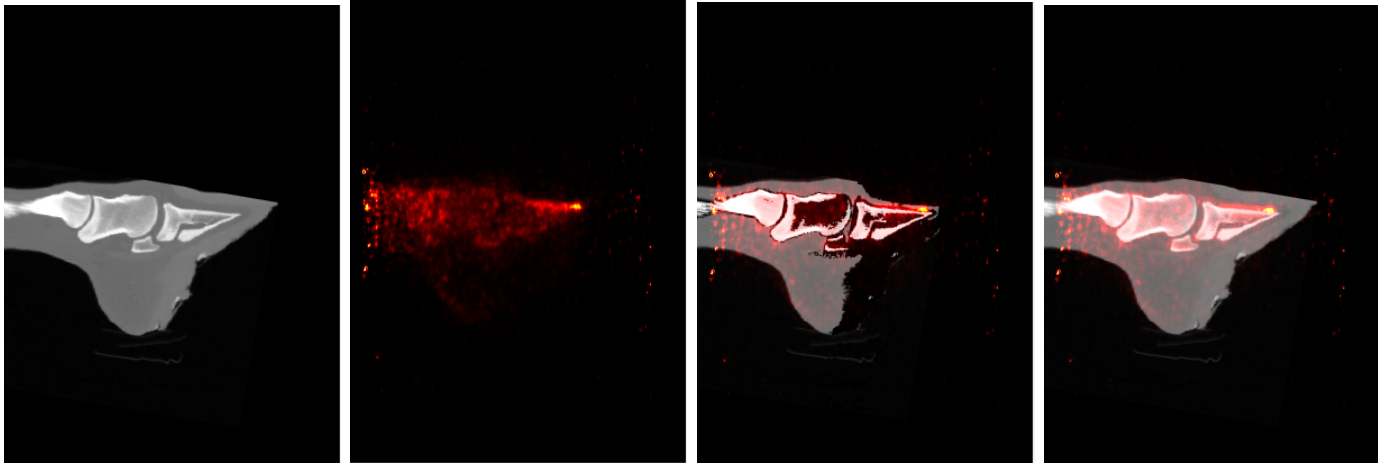


Figure 3.1: (From Left) Original CT, Original PET, segmented CT and PET aligned, Registered original CT and PET images.

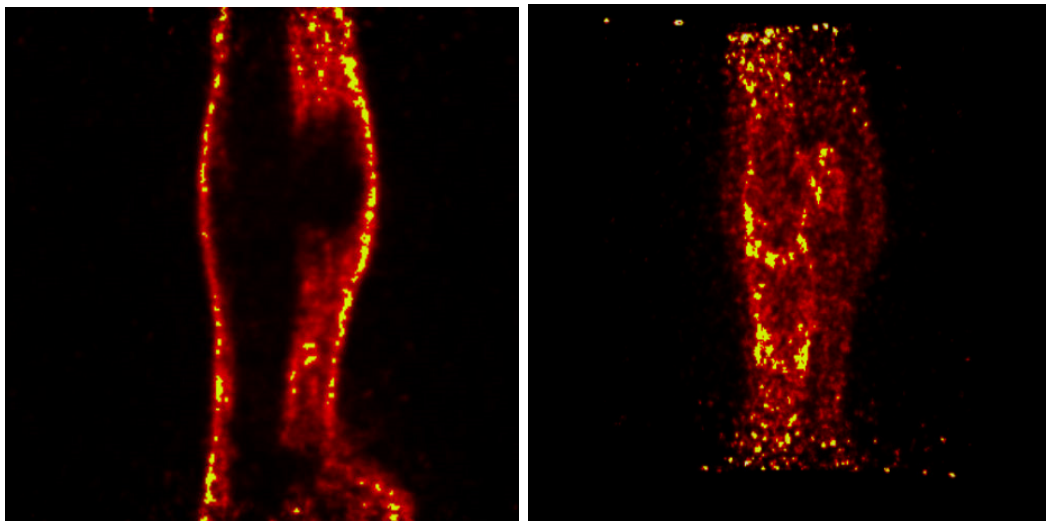


Figure 3.2: (Left) Adult horse, (Right) Young horse

## 3.2 Histogram based thresholding

We will demonstrate the histogram based thresholding technique using the test case shown in Fig. 3.3.



Figure 3.3: CT image before segmentation

Since this is not a bi-modal image, one threshold cannot achieve the required segmentation. We used two thresholds to segment the hoof region. (Refer to section 2.1 on multilevel thresholding). Let us call the thresholds, lower threshold ( $lth$ ) and upper threshold ( $uth$ ). We design  $lth$  to remove the soft tissue regions and the  $uth$  to remove the bone tissues. Since the thresholding technique does not take into consideration the region information, this method is sensitive to noise and intensity inhomogeneities. Hence, to make it more robust, we find the largest connected component in the resultant mask to extract the hoof. Once, a mask is extracted, we

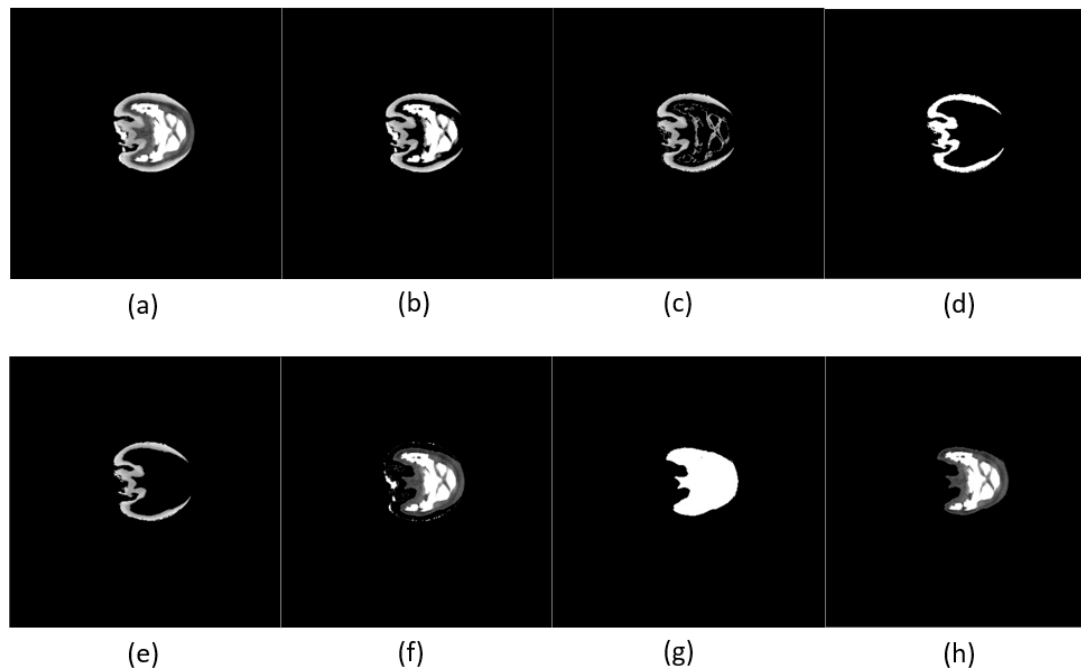


Figure 3.4: Steps in histogram thresholding in CT image.

subtract the mask regions from the original CT to obtain the segmented CT image. The series of steps are shown in Fig. 3.4. (a) Shows the original CT image, (b) shows the result of applying the lower threshold, (c) shows the result of applying the two thresholds, (d) is the largest connected component mask, (e) is the original CT mask, (f) is the segmented CT, (g) is the segmented CT with filtering out the small regions and (h) is the final segmented CT image. The corresponding PET image is shown in Fig. 3.5. The selection of thresholds is demonstrated in Fig. 3.6. More results after applying this algorithm to CT images are as shown in Fig. 3.7.

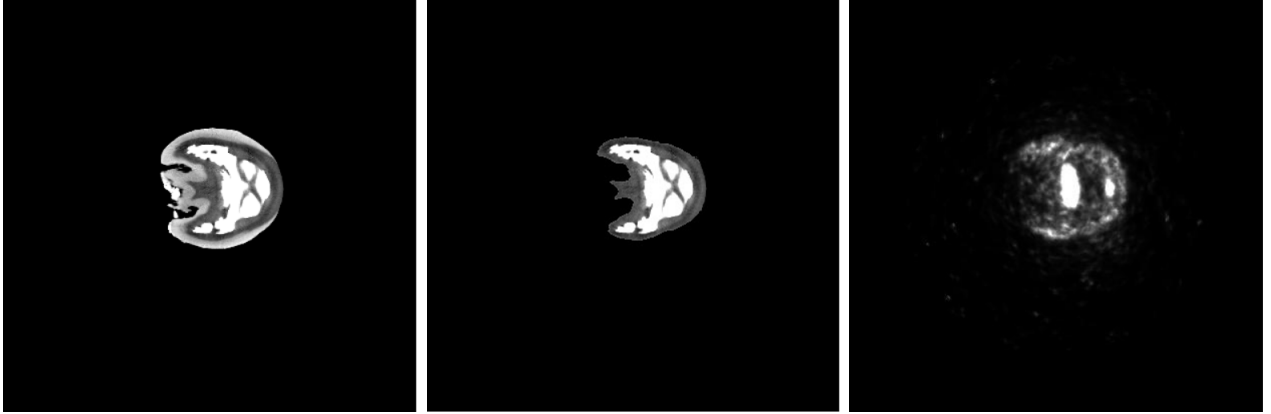


Figure 3.5: (Left) Original CT image, (Middle) Segmented CT ,(Right) Corresponding PET image.

### 3.2.1 Graph-cut based method

Graph-cut methods of image segmentation apply the techniques of graph theory to image processing. Each pixel in an image is considered as a node in the graph. The edges are weighted according to the probability that the pixels are related. We used one type of graph-cut algorithm called the lazysnapping [30]. We draw lines on the image specifying regions of foreground and background called scribbles. The algorithm then computes a graph-cut suggesting the foreground and the background regions.

Fig. 3.8 shows a sample segmentation using the graph-cut method.

The graph-cut problem is posed as a binary labelling problem i.e to assign a unique label to each pixel of the image (1 if the pixel belongs to the foreground and 0 otherwise).

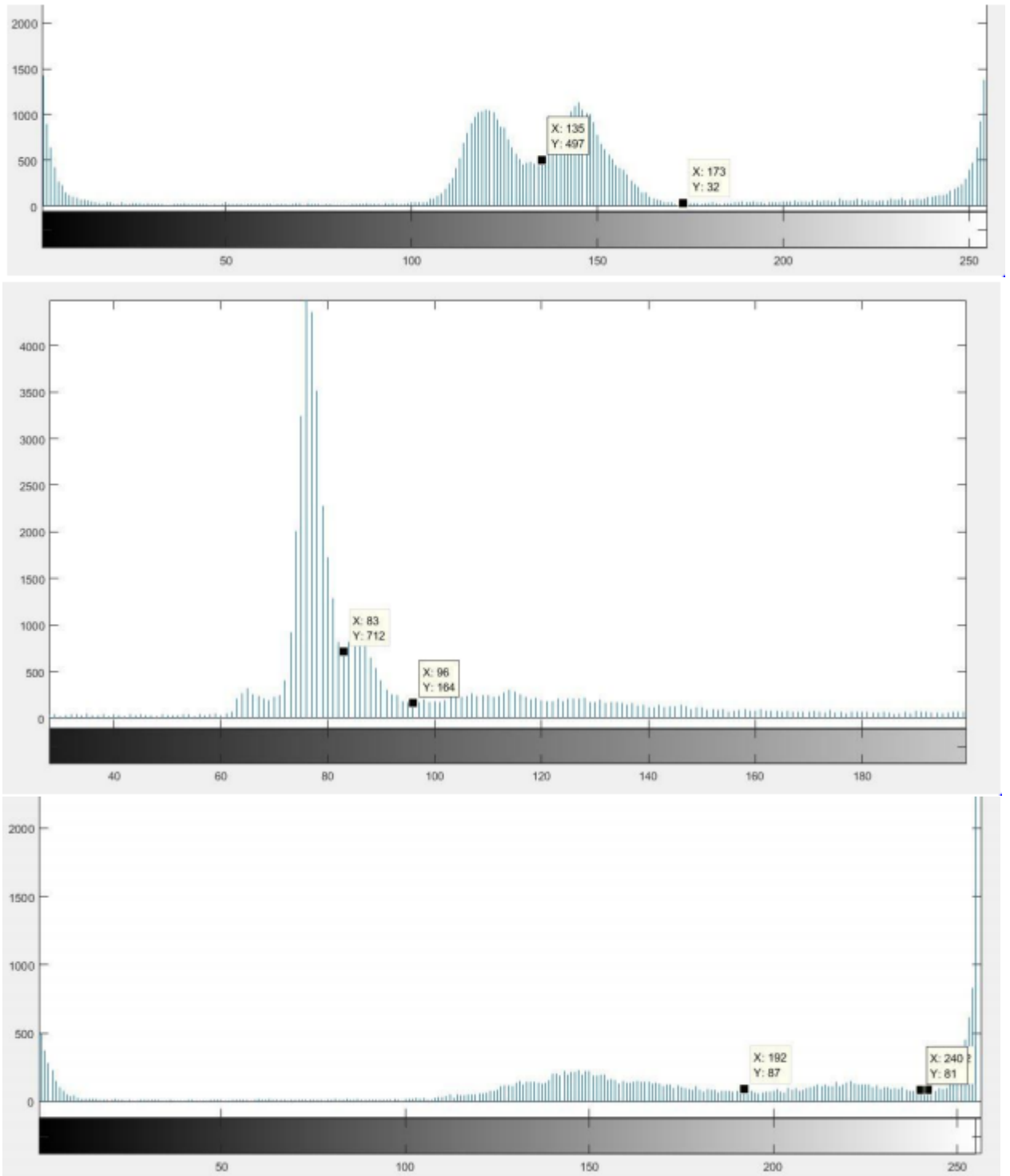


Figure 3.6: Histograms of a CT Images and the selection of thresholds

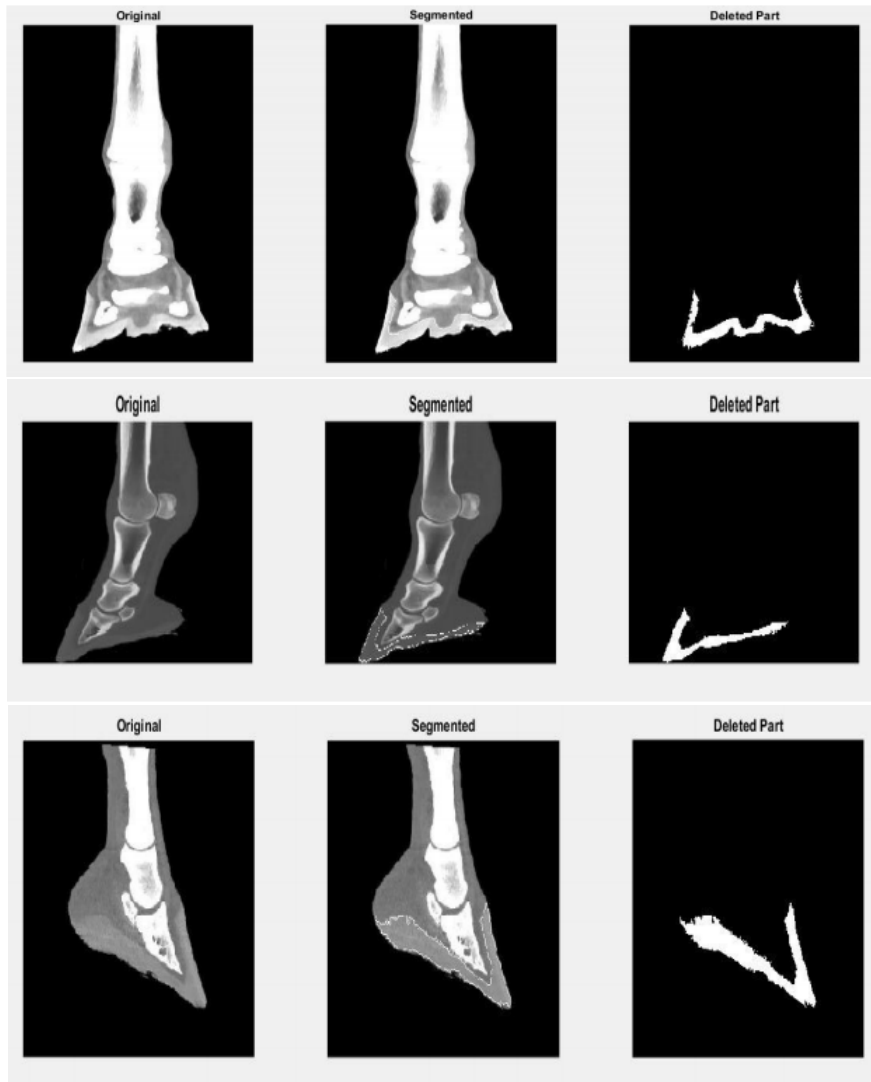


Figure 3.7: Segmentation using histogram-based thresholding

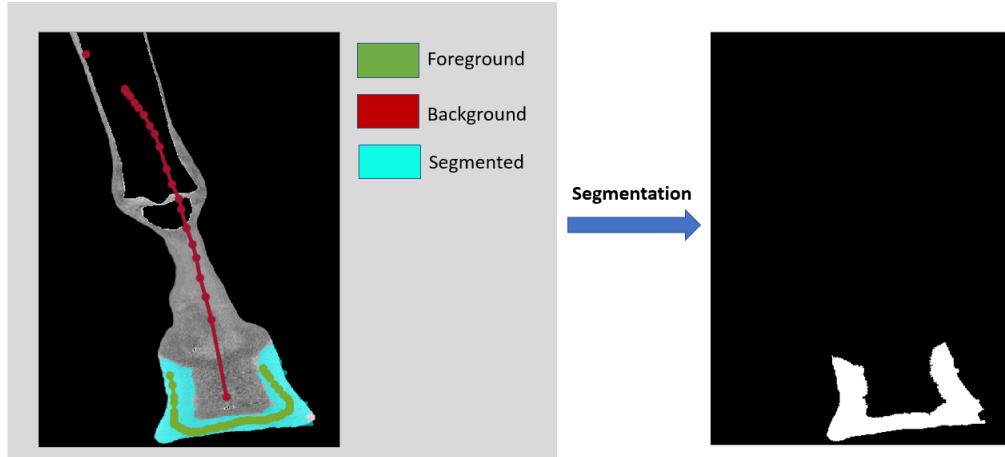


Figure 3.8: Graph-cut Method of Segmentation. The red line indicates the marking as background and the green marker indicates the region marked as foreground.

The solution  $X = \{x_i\}$  can be obtained by minimizing a Gibbs energy  $E(X)$

[12]

$$E(X) = \sum_{i \in \mathcal{V}} E_1(x_i) + \lambda \sum_{(i,j) \in \mathcal{E}} E_2(x_i, x_j) \quad (3.1)$$

where  $E_1(x_i)$  encodes the cost of labelling node  $i$  as  $x_i$  and is called the likelihood energy,  $E_2(x_i, x_j)$  denotes the cost when adjacent nodes  $i$  and  $j$  are labeled as  $x_i$  and  $x_j$  respectively. The energy terms  $E_1$  and  $E_2$  are defined according to the user input. The method of solving the equation is elaborated in [4].

The likelihood energy  $E_1$  indicates if a node belongs to the foreground or background and encodes the color similarity of a node. The colors in seeds in the background and foreground are clustered using the k-means algorithm. [9].  $E_2$  is used to represent energy along the object boundary due to the gradient.  $E_2$  is defined as follows:

$$E_2(x_i, x_j) = |x_i - x_j| \cdot g(C_{ij}) \quad (3.2)$$

where  $g(\xi) = \frac{1}{1+\xi}$  and  $C_{ij} = \|C(i) - C(j)\|^2$  is the  $L_2$ -norm of the RGB color difference of two pixels  $i$  and  $j$ . The  $|x_i - x_j|$  captures the gradient information along the segmentation boundary i.e  $E_2$  is a cost term if the adjacent pixels are allotted to different categories.  $E(X)$  is minimized using the maxflow algorithm described in [3]. The efficiency of this algorithm can be improved by using a pre-segmented image using the watershed transformation. [36].

### 3.2.2 Fast March Algorithm

Level set methods attempt to solve the level-set equation,

$$\Psi_t + F|\nabla\Psi| = 0 \quad (3.3)$$

where  $F$  is a function describing the speed at which the surface should propagate and  $\Psi_t$  is the difference between the current surface and the next surface.  $\gamma(t)$  is the set of points where  $\Psi_t(x, y, t) = 0$ . The solution for  $\gamma(t)$  can be obtained by solving the above equation and then taking the corresponding level set. In this formulation, we find the propagation of an  $N$  dimensional front in terms of the  $N+1$  dimensional front. This gives us the flexibility to deal with the locations of discontinuities. The level set method is an iterative approach to solve the above equation and is computationally very expensive. Fortunately, one constraint on the  $F$  function enables us to use a discretized and optimized algorithm called the Fast-March Method. The constraint implies that the surface should be expanding in only

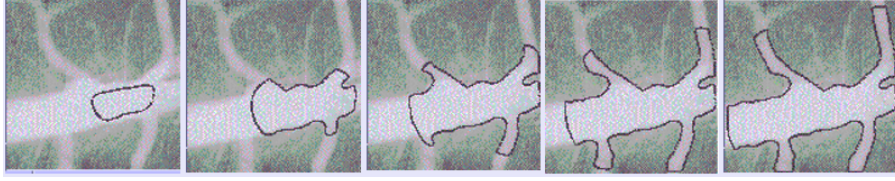


Figure 3.9: Evolving curve using using Fast-March for Image Segmentation[ [1]

one direction which is satisfied by our application.

Let  $F(x,y)$  be the front movement i.e the speed of the front at the point  $(x,y)$ .

Let the front reach the point  $(x,y)$  at  $T(x,y)$ . Then the equation above reduces to

$$|\nabla T|F = 1. \quad (3.4)$$

An algorithm to solve this equation is described in [14]. To use these ideas for image segmentation, the function  $F$  is defined as

$$F(x) = e^{-\tau(|\nabla I(x)|)}, \quad (3.5)$$

where  $|\nabla I(x)|$  is the magnitude of the image gradient at that point and  $\tau > 0$  is a parameter which can be adjusted to define the strength of the function. When the curve passes over points with smaller gradient values, the curve expands quickly and when the curve passes points with higher gradient values, it slows down. An evolving curve is shown in Fig. 3.9 [1].

### 3.3 Results and Discussion

Fig. 3.10 highlights the segmented regions in a CT image.

We have applied the above algorithms on a test data of 15 images. Fig. 3.11

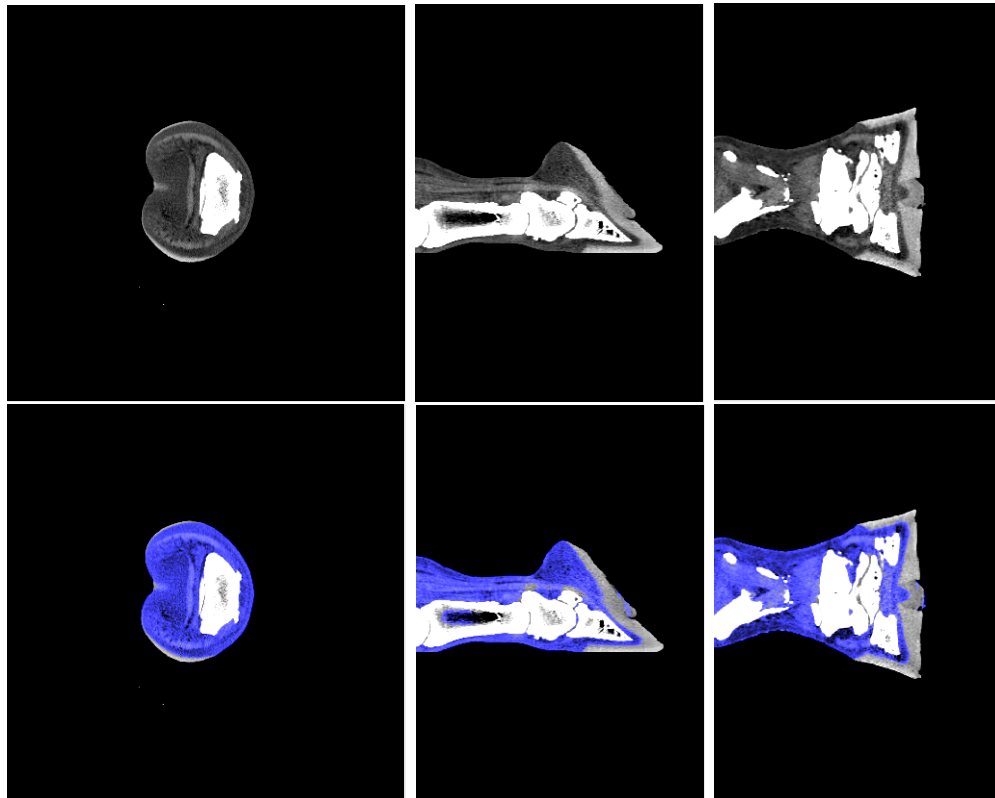
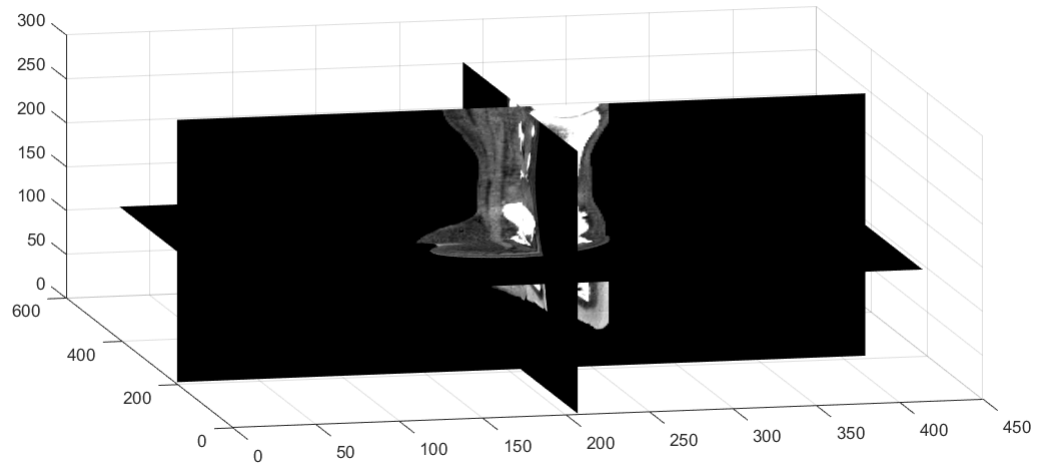


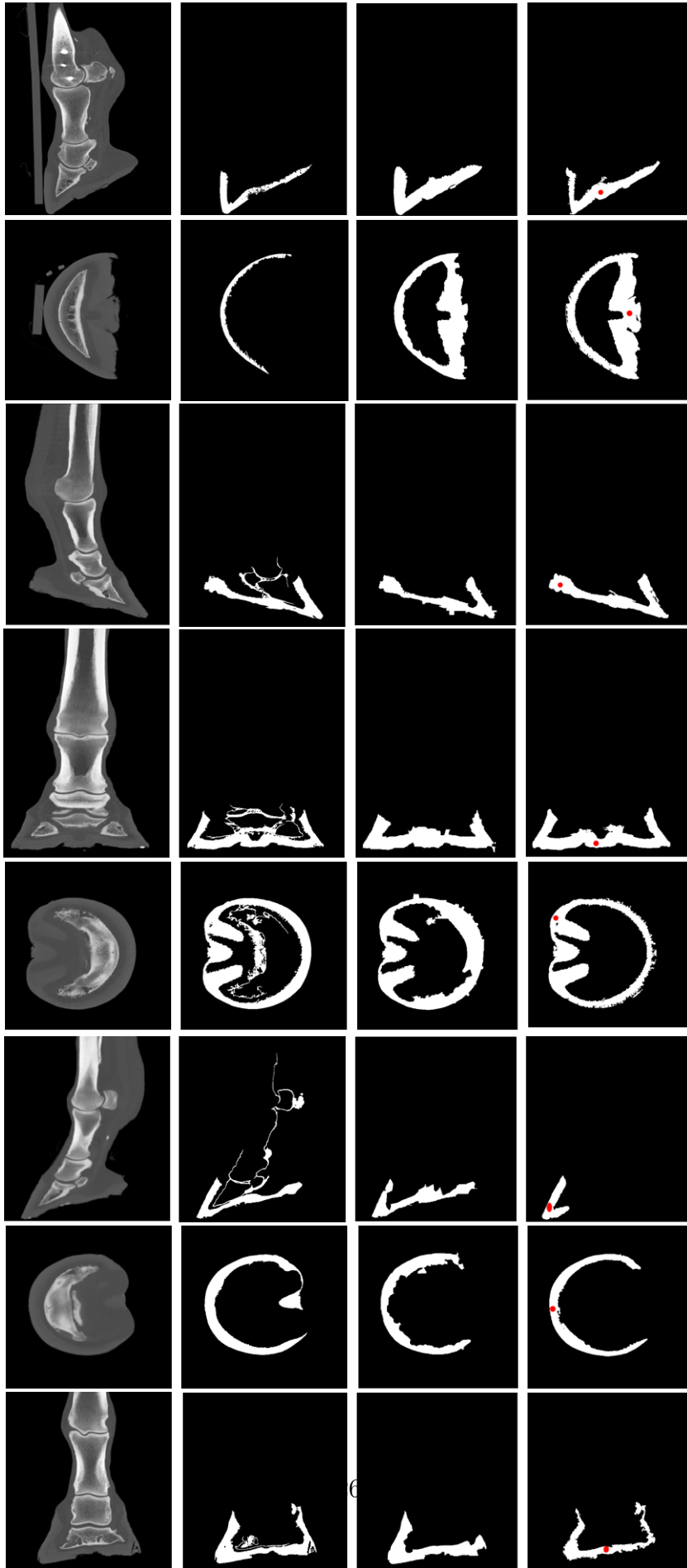
Figure 3.10: Segmentation of CT (3D)

below shows the results of using the algorithms. The first column shows the original images, the second column shows the segmented images using histogram thresholding, the third column shows the result of using graph-cuts while the fourth column shows the results of using the Fast-March Algorithm.

Image segmentation algorithms can be evaluated using different metrics. They can be classified into supervised and unsupervised techniques. In supervised methods, we have a reference image called the "ground truth" which we use to calculate a similarity metric. Unsupervised methods do not require a reference image and evaluate the quality of segmentation based on certain criteria like uniformity of regions segmented, continuity of region interiors etc. A detailed study of the unsupervised methods is presented here [39]. We will evaluate the segmentation using supervised techniques defined below. Our reference image is generated using an interactive segmentation tool for each of these test cases.

Dice coefficient, also called the coincidence Index or similarity index is originally proposed in [8] to quantify the association between two species using a metric which is independent of which species is treated as the base. For images, it can be defined as twice the information present in both the images divided by the sum of information in each of the images. The Dice coefficient ranges from 0 to 1, where 0 implies no association and 1 implies complete association. Information in this case refers to the number of non-zero elements. Fig. 3.12 plots the values of Dice Coefficient for the three methods. It is defined as follows:

Let  $R$  be the ground reference image and  $S$  be the segmented image using a particular algorithm. Let  $N_R$  and  $N_S$  denote the region of foreground of the ground



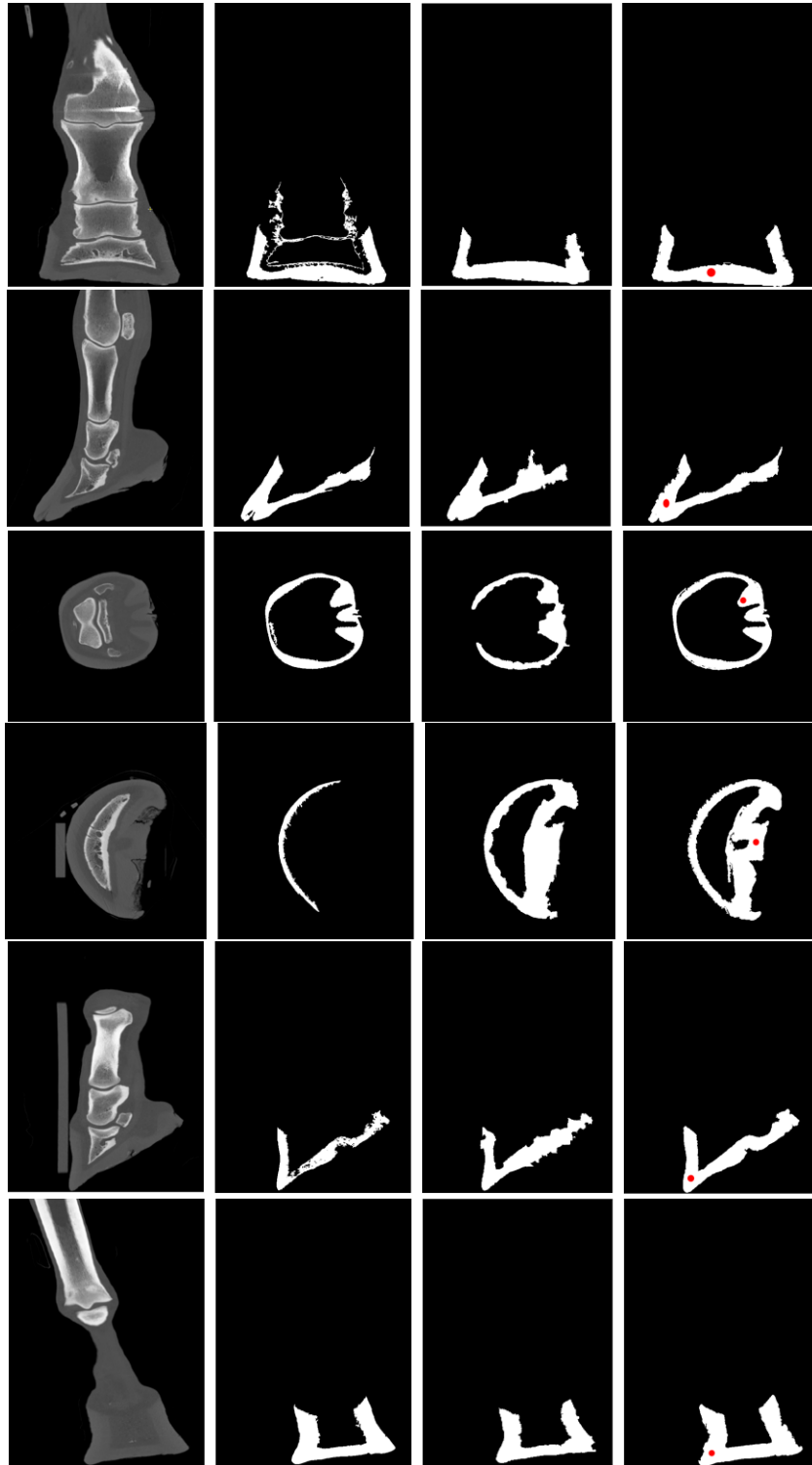


Figure 3.11: The first column shows the original CT images, the second column is the result of segmentation using thresholding, the third column shows Graph-cut method, the fourth column shows Fast-March Algorithm

truth and the segmented image respectively and  $|\cdot|$  denote the number of pixels present in the region.

Dice Similarity index =

$$\frac{2[N_R \cap N_S]}{|N_R| + |N_S|} \quad (3.6)$$

Some other metrics commonly used in the literature to evaluate image segmentation algorithms are as follows [24]:

True Negative Fraction(TNF) =

$$\frac{|N_R \cup N_S|}{|N_R|} \quad (3.7)$$

False Negative Fraction(FNF) =

$$\frac{|N_R - N_S|}{|N_R|} \quad (3.8)$$

True Positive Fraction(TPF) =

$$\frac{|N_S \cap N_R|}{|N_R|} \quad (3.9)$$

False Positive Fraction(FPF) =

$$\frac{|N_S - N_R|}{|N_R|} \quad (3.10)$$

Percentage difference in the area of pixels =

$$\frac{||N_R| - |N_S||}{|N_R|} \times 100 \quad (3.11)$$

Fig. 3.13 plots the percentage difference in area for different test cases using the three segmentation methods.

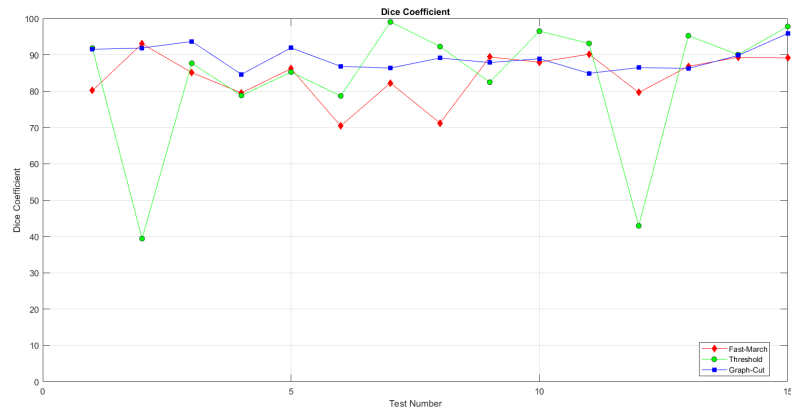


Figure 3.12: Dice Coefficient for the test cases above for three segmentation methods

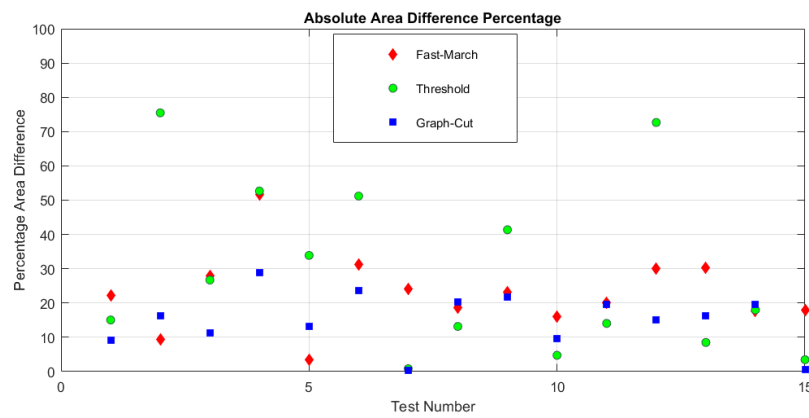


Figure 3.13: Absolute percentage area difference for three segmentation methods

Table 3.1: Dice similarity index for various algorithms.

Subject No.	Fast-March	Threshold	Graph-cut
1	0.8017	0.9185	0.9153
2	0.9305	0.394	0.9187
3	0.8511	0.8767	0.9367
4	0.795	0.7879	0.8463
5	0.862	0.8524	0.9192
6	0.7041	0.7868	0.8681
7	0.8225	0.9905	0.8636
8	0.7122	0.9227	0.8912
9	0.8939	0.8246	0.8785
10	0.8798	0.9652	0.8892
11	0.9017	0.9313	0.8491
12	0.7963	0.4293	0.8648
13	0.8683	0.9527	0.8624
14	0.8932	0.9005	0.8981
15	0.8912	0.9779	0.9587

Table 3.2: True Negative Fraction for different segmentation algorithms

Subject No.	Fast-March	Threshold	Graph-Cut
1	0.9889	0.9184	0.9153
2	0.9830	0.3939	0.9187
3	0.9880	0.8766	0.9366
4	0.9767	0.7879	0.8463
5	0.9760	0.8523	0.9192
6	0.9962	0.7867	0.8680
7	0.9961	0.9904	0.8635
8	0.9898	0.9227	0.8912
9	0.9871	0.8246	0.87841
10	0.98881	0.9652	0.8891
11	0.9856	0.9313	0.8491
12	0.9896	0.9527	0.8623
13	0.9897	0.9005	0.8980
14	0.9880	0.9778	0.9586
15	0.9594	0.4293	0.8648

Table 3.3: False Negative Fraction for different segmentation algorithms

Subject No.	Fast-March	Threshold	Graph-Cut
1	0.0036	0.0050	0.0014
2	0.0036	0.1066	0.00098
3	0.0011	0.00024	0.0004
4	0	0.00020	0.0014
5	0.0188	0.00049	0.0030
6	0.0162	0.00047	0.0011
7	0.0292	0.0014	0.01459
8	0.0213	0.00099	0.0011
9	0.0001	0.00026	0.0014
10	0.0026	0.00063	0.0036
11	0.0005	0.00022	0.0046
12	4.8395E-06	0.00022	0.0023
13	0.00137	0.0090	0.00067
14	0.0016	0.00029	0.0022
15	0.0089	0.0766	0.0073

Table 3.4: True Positive Fraction for different segmentation algorithms

Subject No.	Fast-March	Threshold	Graph-Cut
1	0.8908	0.8493	0.9573
2	0.9744	0.2453	0.9930
3	0.9701	0.9937	0.9895
4	1	0.9954	0.9689
5	0.8763	0.9967	0.9803
6	0.5943	0.9881	0.9711
7	0.7237	0.9862	0.8620
8	0.6459	0.9834	0.9815
9	0.9979	0.9951	0.9741
10	0.9507	0.9881	0.9317
11	0.9918	0.9967	0.9326
12	0.9998	0.9932	0.9322
13	0.9725	0.8194	0.9865
14	0.9710	0.9948	0.9614
15	0.9155	0.2733	0.9301

Table 3.5: False Positive Fraction for different segmentation algorithms

Subject No.	Fast-March	Threshold	Graph-Cut
1	0.0110	2.4278E-06	0.0044
2	0.0169	0	0.0238
3	0.0119	0.0105	0.0047
4	0.0232	0.0239	0.0144
5	0.0239	0.0522	0.0233
6	0.0037	0.0210	0.0106
7	0.0038	0.0005	0.0142
8	0.0101	0.0089	0.0133
9	0.0128	0.0228	0.0133
10	0.0111	0.0031	0.0087
11	0.0143	0.0099	0.0182
12	0.0103	0.0031	0.0078
13	0.0102	0.00002	0.0105
14	0.0119	0.0022	0.0025
15	0.0405	0	0.0233

## Chapter 4: Image Registration of Equine PET and CT Images

An image registration algorithm finds a transformation that can be applied on the source image to register with the target image. Throughout this thesis, we assume that the PET image is the target image and the CT image is the source or moving image. Hence, our aim is to find a transformation to apply on the CT image which registers it with the PET image.

There are two broad classes of transformations: Rigid and Non-rigid. Similar to the idea of a rigid body, rigid transformation assures that the relative position of the pixels is maintained. Thus, a rigid transformation can only include rotation, translation and reflection. Allowing for the scaling parameters results in a similarity transformation with four parameters in two dimensions. Further relaxation to include the skew operations results in an affine transformation with six degrees of freedom in two dimensions. Non-rigid transformations on the other hand, have no restrictions and in the extreme case, can deal with an infinitely deformable object with infinite parameters. Such transformations are achieved by estimating the transformation vectors at each pixel. We will discuss multimodal image registration using rigid transformation in the next sections and formulate a deformable registration problem for equine PET and CT images.

## 4.1 Registration using Fiducial Points

### Fiducial points

Fiducial points are markers used in images as points of reference. Given few sets of fiducial points, we can estimate a transformation. The exact number of points required to estimate the transformation depends on the type of transformation used. For example, affine transformations would have six unknown parameters and requires atleast six pairs of fiducial points else it will result in an underdetermined system with infinite number of solutions. If we have more number of fiducial points, we have an overdetermined system of equations, and we need a criteria to fit the data into the transformation. This problem is called the absolute orientation problem. [15] One criterion used, is to minimize the difference between the target points and the transformed points in the least squares sense. [35] . Fig. 4.1 shows a pattern of 2D source points which need to be transformed to match a pattern of target points. We design a similarity transformation (Rotation  $R$ , translation  $t$  and Scaling  $c$ ) as follows: The lemma follows from [35].

Lemma: Given a set of source points  $\{\mathbf{x}_1, \mathbf{x}_2, \mathbf{x}_3, \dots, \mathbf{x}_n\}$  and a set of target points  $\{\mathbf{y}_1, \mathbf{y}_2, \mathbf{y}_3, \dots, \mathbf{y}_n\}$  in a  $m$ -dimensional space ( $m=2$  or  $m=3$ ), the optimum transformation parameters are obtained from

$$R = USV^T \quad (4.1)$$

$$t = \mu_y - cR\mu_x \quad (4.2)$$

$$c = \frac{1}{\sigma_x^2} tr(DS) \quad (4.3)$$

where

$$AB^T = UDV^T \quad (4.4)$$

$$S = \begin{cases} I & \text{if } \det(U)\det(V) = 1 \\ \text{diag}(1, 1, \dots, 1, -1) & \text{if } \det(U)\det(V) = -1 \end{cases}$$

when  $\text{rank}(\sum_{xy}) = m - 1$  and

$$S = \begin{cases} I & \text{if } \det(\sum_{xy}) \geq 0 \\ \text{diag}(1, 1, \dots, 1, -1) & \text{if } \det(\sum_{xy}) < 0 \end{cases}$$

when  $\text{rank}(\sum_{xy}) \geq m - 1$

and  $\sum_{xy}$  is a covariance matrix of X and Y,  $\mu_x$  and  $\mu_y$  are mean vectors of X and Y,  $\sigma_x^2$  and  $\sigma_y^2$  are variances of X and Y. X and Y are  $m \times n$  matrices created from the data points. Fig. 4.2 shows the transformed source points using the similarity transformation designed above and the target points. Observe that though we do not reach the exact location of the target points, we can approximately satisfy all the pattern constraints.

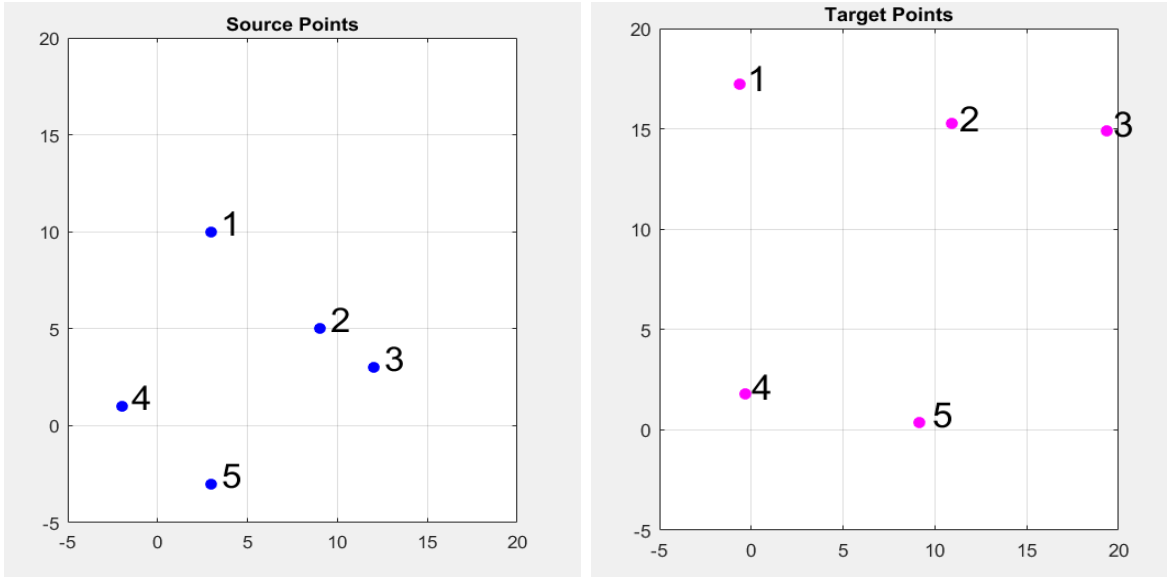


Figure 4.1: (left) Source Points, (Right) Target Points

The same can be extended to a 3D volume. Fig. 4.3 shows two 3D images where the user is allowed to select pairs of matched points by visual inspection. We then use these points to estimate a similarity transformation and the result is as shown in Fig. 4.4. There is a possibility of small deviations in the coordinates of the points due to human errors. We will see how the transformation parameters change with some deviation from a fixed point. Table.5.1 shows how the Euler-Rodriguez parameters [7] change with varying noise(N).

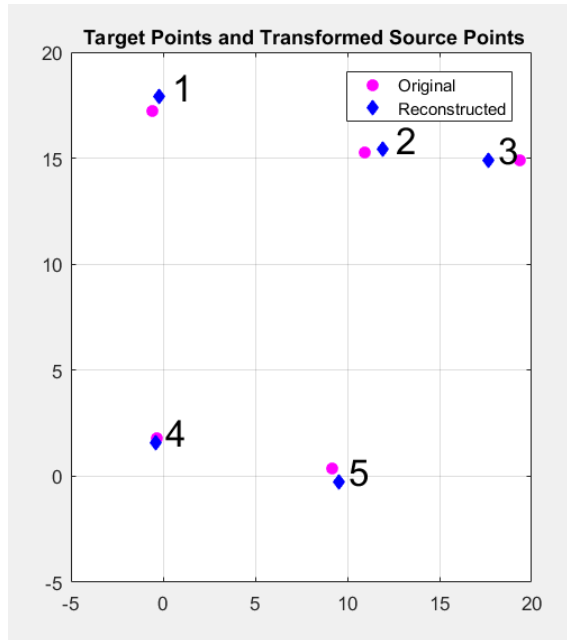


Figure 4.2: (left) Transformed Image, (Right) Original Target Image

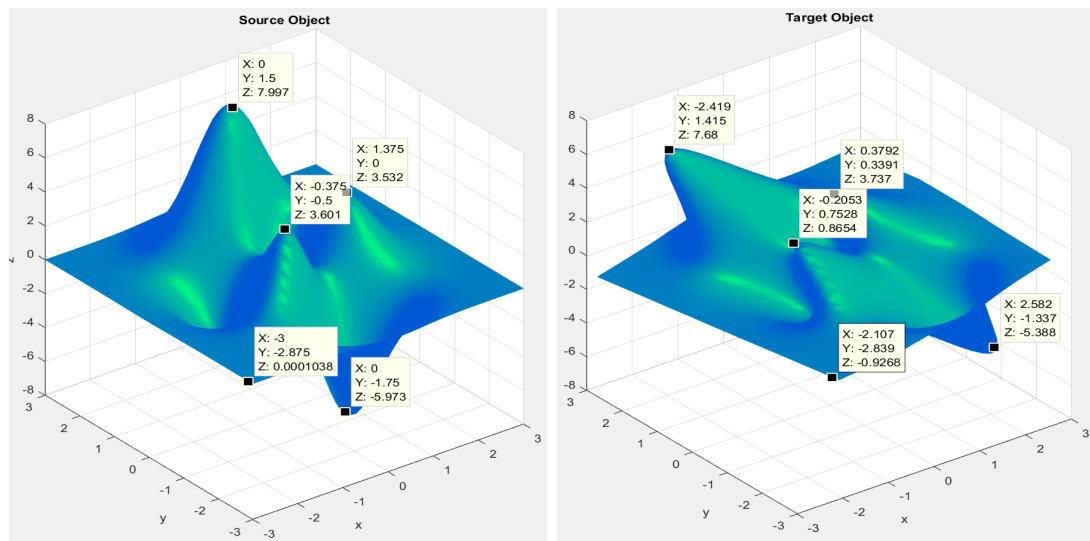


Figure 4.3: (Left) Source Object , (Right) Target Object

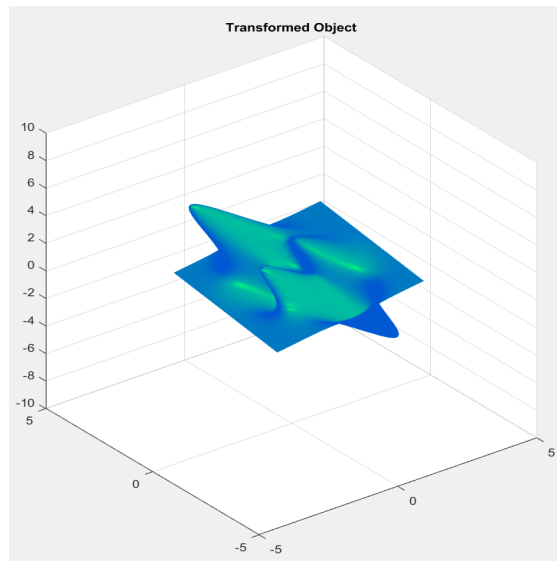


Figure 4.4: (Left) Transformed Object, (Right) Original Target Image

Table 4.1: The points taken are  $(3, 10, 2)$ ,  $(9, 5, 1)$ ,  $(12, 3, 4)$ ,  $(-2, 1, -1)$ ,  $(3, -3, 3)$ . The third point is changed as  $(x + N/2, y + N, z + 3N/2)$ .  $\alpha$ ,  $\beta$  and  $\gamma$  are the Euler Angles in Radians.  $e_1$ ,  $e_2$ ,  $e_3$  and  $\theta$  are Rodriguez parameters.

N	C	Tx	Ty	Tz	$\alpha$	$\beta$	$\gamma$	e1	e2	e3	$\theta$
0	1.5	3	2	1	0.314	0.52	0.78	0.094	0.66	0.74	0.91
0.1	1.502	3.012	2.004	0.986	0.312	0.517	0.785	0.0951	0.658	0.743	0.913
0.2	1.506	3.037	2.013	0.959	0.307	0.505	0.785	0.096	0.646	0.748	0.908
0.3	1.512	3.075	2.026	0.919	0.301	0.488	0.784	0.098	0.627	0.756	0.900
0.4	1.521	3.129	2.043	0.869	0.293	0.465	0.784	0.100	0.603	0.766	0.891
0.5	1.533	3.198	2.063	0.808	0.283	0.437	0.784	0.103	0.572	0.778	0.880
0.6	1.549	3.286	2.084	0.741	0.271	0.404	0.784	0.106	0.536	0.791	0.868
0.7	1.568	3.394	2.106	0.668	0.258	0.367	0.785	0.109	0.494	0.806	0.856
0.8	1.592	3.524	2.128	0.594	0.243	0.326	0.786	0.112	0.448	0.821	0.844
0.9	1.621	3.676	2.148	0.522	0.226	0.283	0.789	0.114	0.397	0.836	0.833
1	1.655	3.852	2.164	0.455	0.209	0.237	0.790	0.116	0.343	0.851	0.824

We now demonstrate the use of fiducial points on a PET-CT image pair. The user selected points are shown in Fig. 4.5, the correspondence between the respective pair of points is shown in Fig. 4.6 and the result obtained is shown in Fig. 4.7.

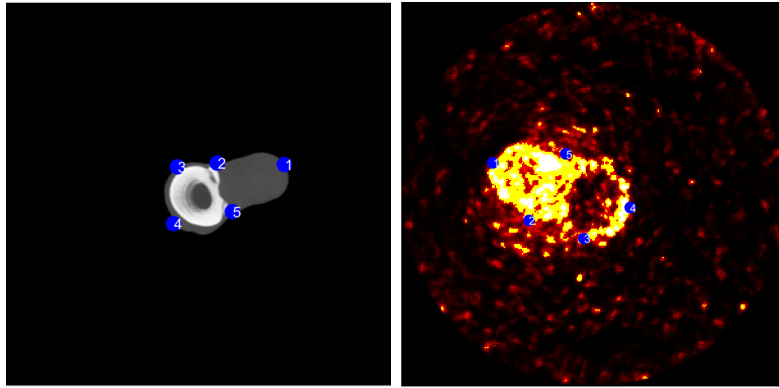


Figure 4.5: (left) Data points on CT Image, (Right) Data points on PET Image

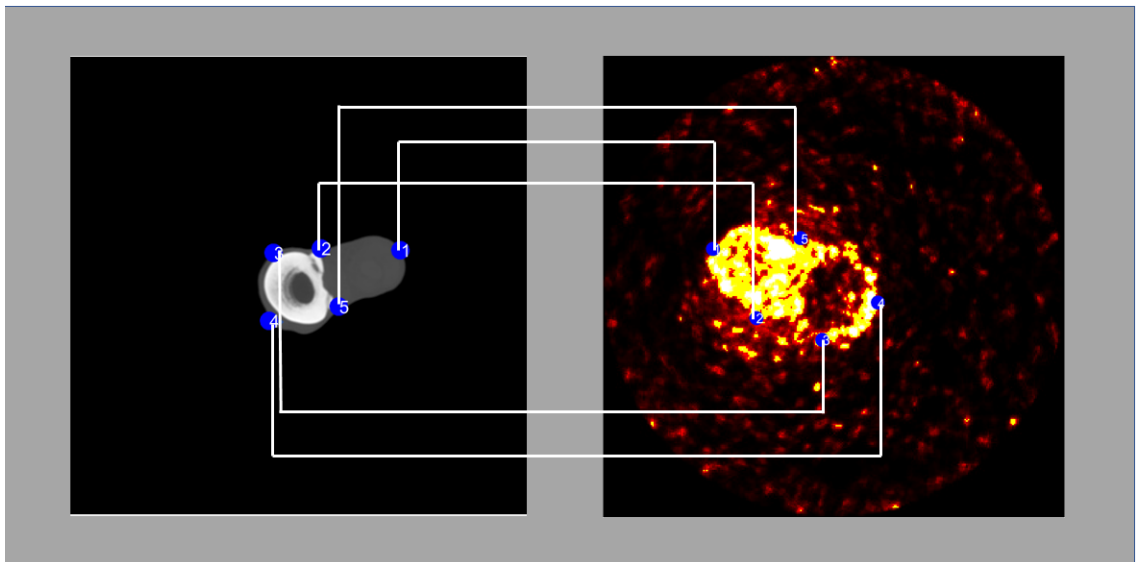


Figure 4.6: The lines show the correspondence between points chosen on CT(Left) and PET(Right)

The transformation parameters calculated are as shown in the table.

Table 4.2: Source and Target Fiducial Points

X(Source)	Y(Source)	X(Target)	Y(Target)	X new	Y new
371	217	72	126	67.1166	123.3772
282	215	100	171	109.6826	167.1735
229	220	143	185	138.0095	190.2265
224	296	179	161	177.0187	155.4617
302	280	129	119	131.1726	125.7611

Table 4.3: Transformation Parameters for PET-CT pair

Scale	Tx	Ty	Theta(Radians)
0.6860	144.1669	407.9968	2.3644

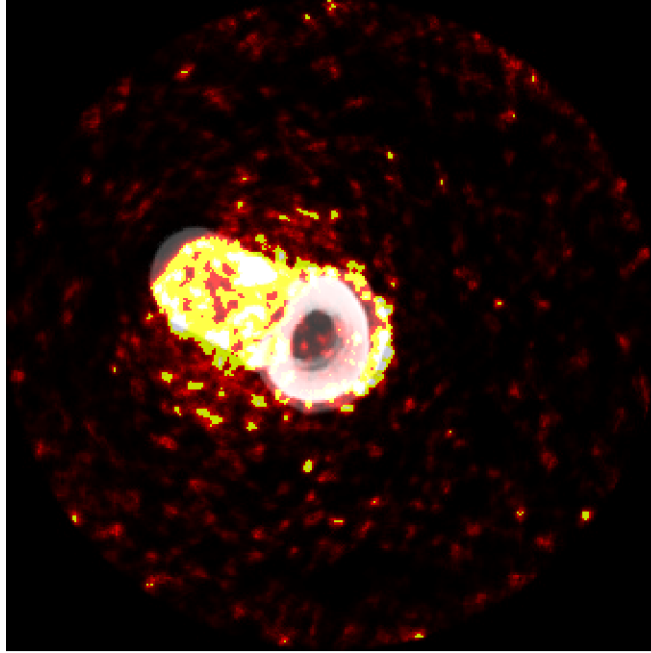


Figure 4.7: Registration using Fiducial points given.

Registration using fiducial points can be used as a supplemental technique to automatic multi-modal image registration. It can be used to fine tune the registration as well.

In fiducial points-based registration, we will need a human to input and monitor the registration continuously. Even for a very experienced person, this process might take a few hours to complete registration with acceptable accuracy. Hence, we try to use an automatic registration algorithm that can ease the whole process of registration. In the next section, we will discuss an entropy-based similarity metric called the mutual information.

## 4.2 Registration using Mutual Information

Mutual information of two random variables is the amount of information one variable can provide about the other. Mutual Information is used as the similarity measure in multi-modal image registration in the field of medical imaging. [16]. Higher mutual information implies better registration as shown in the Fig. 4.8. It is calculated using the individual and joint entropies of the two images using the joint histogram.

If  $u$  and  $v$  are any two random variables, mutual information is calculated as follows [16]:

$$I(U, V) = \sum_{u,v} p_{UV}(u, v) \log \frac{p_{UV}(u, v)}{p_U(u)p_V(v)} \quad (4.7)$$

where  $p_U(u)$  and  $p_V(v)$  are the marginal probability distributions and  $p_{UV}(u, v)$  is the joint probability distribution. When the variables  $U$  and  $V$  are statistically independent,  $p_{UV}(u, v) = p_U(u).p_V(v)$  and mutual information is zero, i.e knowing information about one variable does not help in estimating the other variable.

Let  $x$  and  $y$  be the voxel intensities of PET and CT images respectively. Let  $h(x)$ ,  $h(y)$  be the histograms of the two images and  $h(x, y)$  be the joint histogram of the two images.

Define entropy of PET image as

$$H(X) = - \sum_x p_X(x) \log(p_X(x)) \quad (4.8)$$

and entropy of CT image as

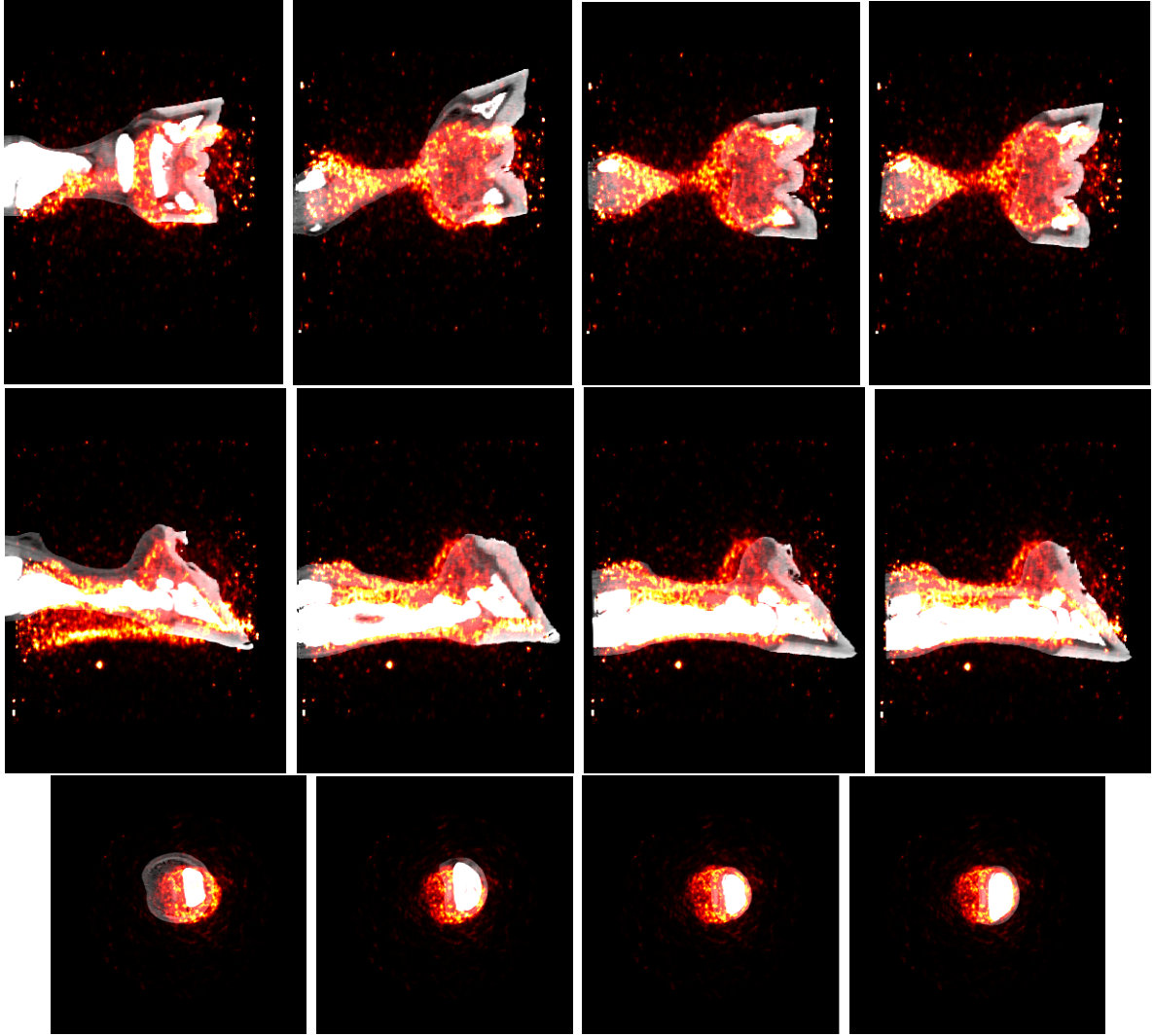


Figure 4.8: The figure demonstrates the change in mutual information value and the registration performance. Higher mutual information implies better registration. From left to right, the similarity percentages calculated are 25.4, 36.8, 44.8 and 45.1.

$$H(Y) = - \sum_y p_Y(y) \log(p_Y(y)) \quad (4.9)$$

Then the mutual information is defined as

$$MI(X, Y) = H(X) + H(Y) - H(X, Y) \quad (4.10)$$

Mutual information is robust in the sense that there are no assumptions on the image intensities, and no assumption about the image content in different modalities. The probable parameters of the geometric transformation are estimated from an initial estimate. The initial estimate could either be random or from any previous registration method. We will use the center of intensities as the initial estimate of the transformation parameters.

Interpolation at higher orders do not result in significant improvements in registration whereas quadratic and cubic interpolation gives significantly better consistent results than linear. [23]. A non-linear optimization technique called one-plus-one evolution algorithm used to solve this is described in Appendix B of [32]. The multiresolution Image Pyramid is as shown in Fig. 4.9

The value of the transformation parameters are obtained iteratively as follows:  
[16]

$$\phi^{n+1} = \phi^n \pm w^* \Delta\phi \quad (4.11)$$

where  $\phi^n$  is the parameter at the  $n^{th}$  iteration. Let  $M$  be the moving Image,  $F$  be the fixed Image and  $M(\phi^n)$  denote the Image after transforming  $M$  using the parameter at  $n^{th}$  iteration. Let  $I(F, M(\phi^n))$  denote the mutual information between the fixed and moving Image transformed after  $n^{th}$  iteration. The weight value  $w^*$  is given by

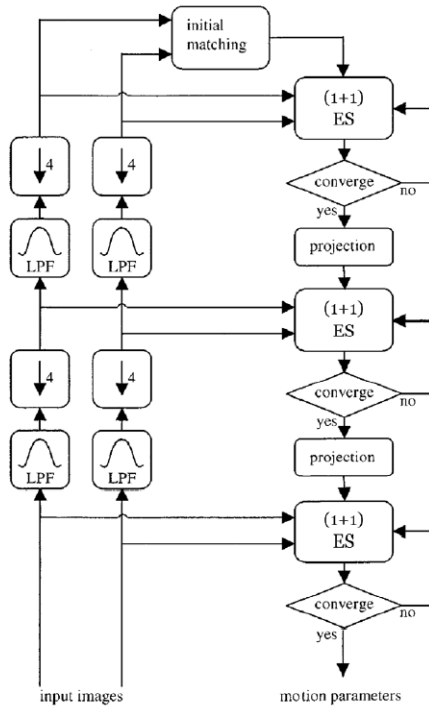


Figure 4.9: Multiresolution Image Pyramid [11]

$$w^* = \begin{cases} \frac{1}{w} & \text{if } I(F, M(\phi^n)) \geq I(F, M(\phi^{n-1})) \\ w & \text{otherwise} \end{cases}$$

where  $w = \frac{I(F, M(\phi^{n-1}))}{I(F, M(\phi^n))}$ . We will see that the parameters converge to a final value after several iterations.

### 4.3 Registration using Edge Information

The motivation to use edge information in the registration process is two-fold. One is the sparsity of the matrix values and the other is the reduced redundancy in the image. Observe that in a CT image, there is a lot of redundant information i.e in grey level intensities. Our aim is to somehow find a transformation to the CT image which can be applied on the original CT image to achieve registration. Instead of using the CT image, we use the edge image of the CT and align it with the edge image of the PET.

One of the main challenges is to extract the edges in the images. Edge detection in a CT image is straight forward whereas edge detection in a PET image requires some preprocessing since PET images are generally very noisy.

Edges in images are detected by computing the gradient magnitudes. Different gradient operators are used for edge detection like the ones proposed by Roberts [4.13], Prewitt [4.14] and Sobel [4.15].

$$G_x = \begin{bmatrix} 0 & 1 \\ -1 & 0 \end{bmatrix}; G_y = \begin{bmatrix} 1 & 0 \\ 0 & -1 \end{bmatrix} \quad (4.13)$$

$$G_x = \begin{bmatrix} -1 & 0 & 1 \\ -1 & 0 & 1 \\ -1 & 0 & 1 \end{bmatrix}; G_y = \begin{bmatrix} -1 & -1 & -1 \\ 0 & 0 & 0 \\ 1 & 1 & 1 \end{bmatrix} \quad (4.14)$$

$$G_x = \begin{bmatrix} -1 & 0 & 1 \\ -2 & 0 & 2 \\ -1 & 0 & 1 \end{bmatrix}; G_y = \begin{bmatrix} -1 & -2 & -1 \\ 0 & 0 & 0 \\ 1 & 2 & 1 \end{bmatrix} \quad (4.15)$$

These operators are applied on the image pixels to compute the gradients in orthogonal directions and threshold the gradient magnitude to recover an edge. The gradient operators do high pass filtering on the images thus amplifying high frequency noise. Prewitt and Sobel kernels reduce the effect of noise by computing the horizontal and vertical differences of local sum.

To compute the edges in a volume, the first step is to compute the partial gradient for each axis. The partial gradient vector is given by:

$$\nabla f = \left( \frac{\partial f}{\partial x}, \frac{\partial f}{\partial y}, \frac{\partial f}{\partial z} \right)$$

We will apply a 3x3x3 kernel to compute the partial derivatives. Let  $H_x, H_y$  and  $H_z$  be the x, y and z direction kernels given by

$$H_x(m, n, p) = \left[ \left[ \begin{bmatrix} -1 & -3 & -1 \\ -3 & -6 & -3 \\ -1 & -3 & -1 \end{bmatrix}, \begin{bmatrix} 0 & 0 & 0 \\ 0 & 0 & 0 \\ 0 & 0 & 0 \end{bmatrix}, \begin{bmatrix} 1 & 3 & 1 \\ 3 & 6 & 3 \\ 1 & 3 & 1 \end{bmatrix} \right] \quad (4.16)$$

$$H_y(m, n, p) = \left[ \left[ \begin{bmatrix} 1 & 3 & 1 \\ 0 & 0 & 0 \\ -1 & -3 & -1 \end{bmatrix}, \begin{bmatrix} 3 & 6 & 3 \\ 0 & 0 & 0 \\ -3 & -6 & -3 \end{bmatrix}, \begin{bmatrix} 1 & 3 & 1 \\ 0 & 0 & 0 \\ -1 & -3 & -1 \end{bmatrix} \right] \quad (4.17)$$

$$H_z(m, n, p) = \left[ \begin{array}{c} \left[ \begin{array}{ccc} -1 & 0 & 1 \\ -3 & 0 & 3 \\ -1 & 0 & 1 \end{array} \right], \left[ \begin{array}{ccc} -3 & 0 & 3 \\ -6 & 0 & 6 \\ -3 & 0 & 3 \end{array} \right], \left[ \begin{array}{ccc} -1 & 0 & 1 \\ -3 & 0 & 3 \\ -1 & 0 & 1 \end{array} \right] \end{array} \right] \quad (4.18)$$

We shift the above gradient operators across the voxels and compute an inner product. Let the inner products obtained be  $g_x(m, n, p)$ ,  $g_y(m, n, p)$  and  $g_z(m, n, p)$ . The square of the gradient vector magnitude is given by

$$g(m, n, p)^2 = g_x(m, n, p)^2 + g_y(m, n, p)^2 + g_z(m, n, p)^2 \quad (4.19)$$

We set a threshold for this gradient vector magnitude to compute the edges in a volume. It has been observed that Sobel operators provide a very good estimate of the gradients and are also effective in reducing the noise and aliasing artefacts. A good study of the edge detection algorithms is presented in [25]. We will use the 3D Sobel edge detector to detect edges in PET and CT images. The next two sections discuss edge detection in PET and CT images. Once we obtain the edges of both the images, we will discuss the metric used and the method of alignment.

### 4.3.1 Edge Detection in PET images

Before we try to detect edges in the PET image, we observe that the PET image is very noisy. We hence apply a smoothing or averaging filter of high order (15) to compensate noise. The resultant PET image is as shown in Fig. 4.10 (middle). Since, the image is much smoother now, we use the standard edge detection techniques discussed in the previous section. Our aim is to obtain the edges of the

bone and soft tissue regions. Direct application of edge detection has the result as shown in Fig. 4.10 (right). To improve this further, we will detect the inner and outer edges separately. The algorithm is described in Fig. 4.11.



Figure 4.10: (Left) Original PET Image, (Middle) Filtered PET Image, (Right) Direct Edge Detection on PET Image

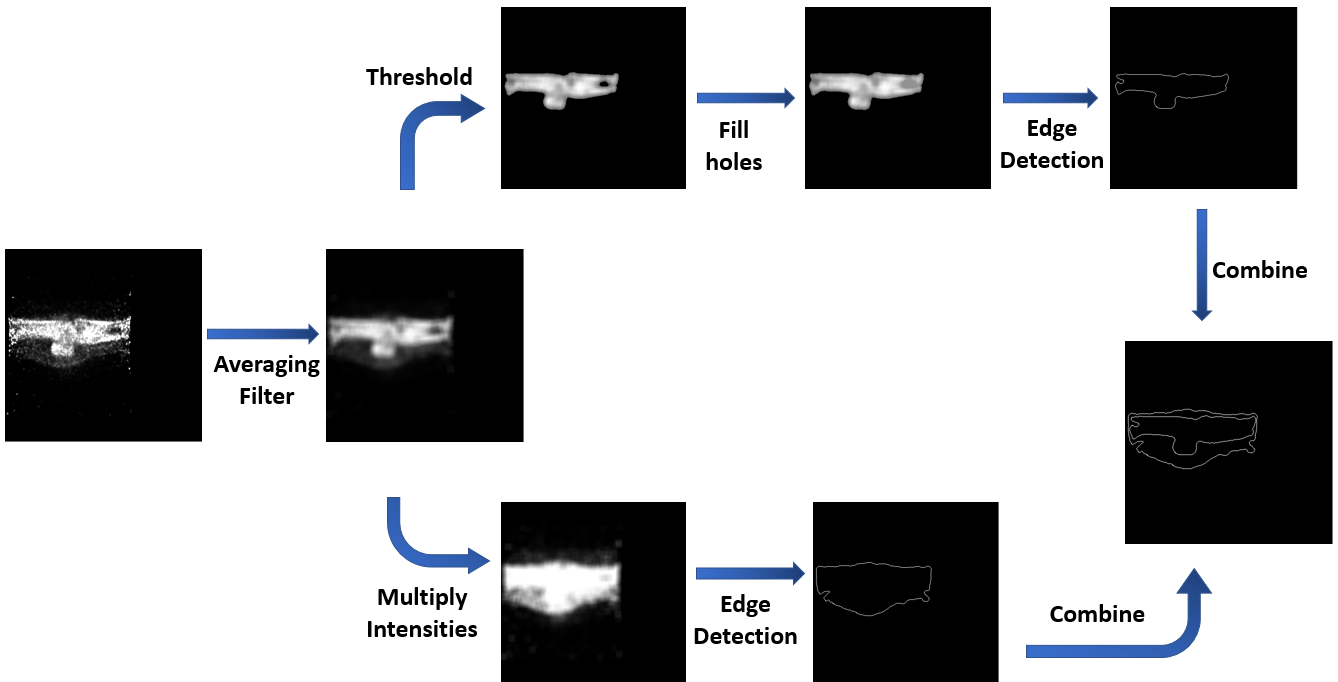


Figure 4.11: Edge Detection on PET Image

### 4.3.2 Edge Detection in CT images

Direct edge detection on the image has resulted in an edge as shown in Fig. 4.12. For improved edge detection, we have separately identified the inner and outer edges. The CT images are not noisy, hence did not require any smoothing filter. We would like to have two clear boundaries for the bone and the tissue hence use the method used above in the case of PET images to detect boundaries and the final result is as shown in Fig. 4.13. The steps are described below.

1. Contrast stretch the original Image to cover the entire intensity range and threshold the image at nearly 100 to have the bone region separated. Fill

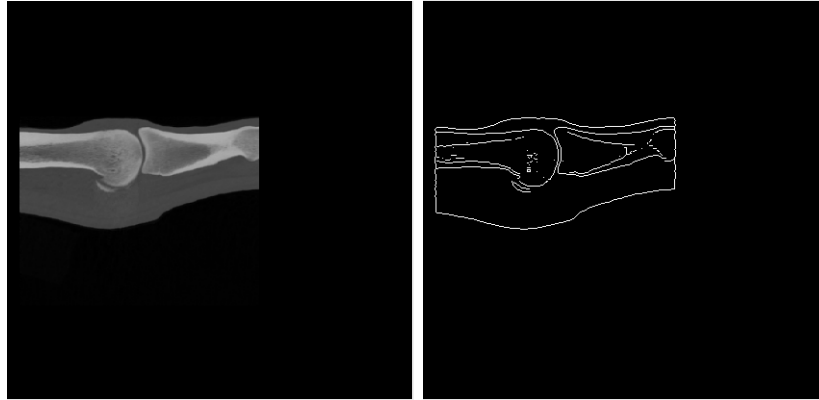


Figure 4.12: (Left) Original CT, (Right) Direct Edge Detection in CT Image

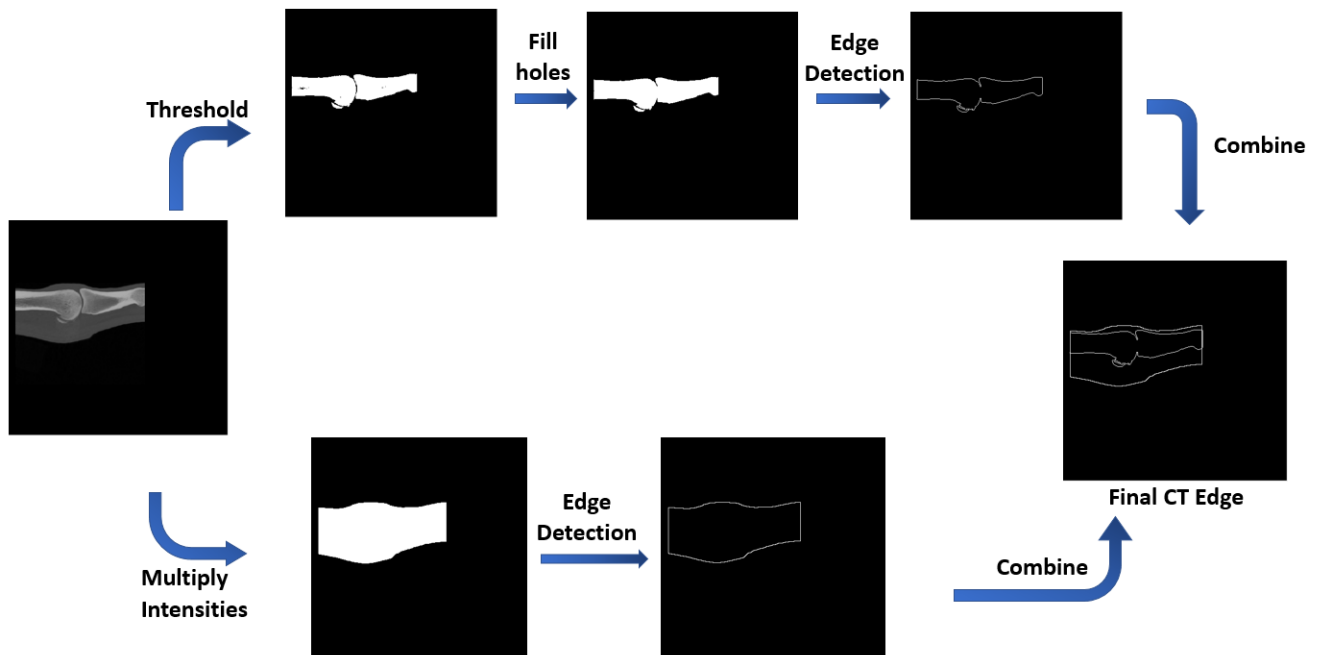


Figure 4.13: Edge Detection in CT images

holes in the binary image obtained and perform edge detection.

2. Multiply the image intensities by a large number (say 10) to obtain a binary image which on edge detection gives the outer boundary of CT image.
3. Combine the edges obtained in step 1 and 2 to get the final boundary image.

We now use the edge images of CT and PET as the new moving and fixed images respectively in our registration problem. Since we have only binary images, the metric for alignment can be simplified. It can be taken as the logical AND of the two images, for example. The two edge images are shown in Fig. 4.14.

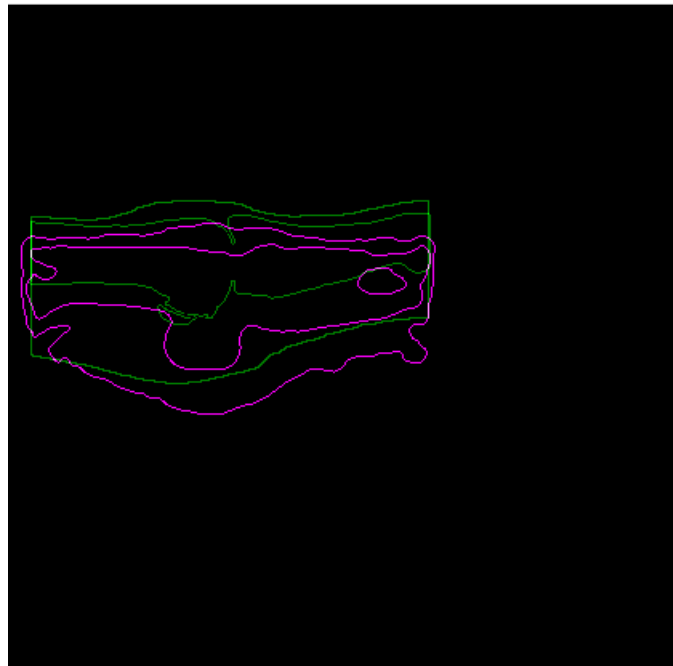


Figure 4.14: The pink lines show the edges of a PET image and the green lines show the edges in a CT image.

The PET and CT edges detected in the above sections are aligned using the

translation parameter search. The new metric is the number of ones in the result obtained by performing logical AND on both the binary images. Fig. 4.15 shows the result of using the translation parameters search.

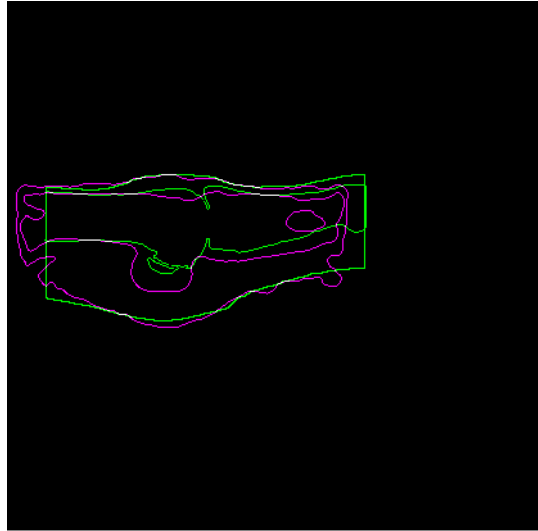


Figure 4.15: Edge Alignment using the Edge Metric and Translational Parameters search

#### 4.4 Some Results

Providing a good initial condition is important for the fast convergence of any registration algorithm. One such good initial transformation is given by matching the center of intensities of the PET and CT images. This is discussed in detail in Chapter 5 in the coarse registration section.

One example of a PET-CT registration is shown in Fig. 4.16. The center slices on each axis is shown. Fig. 4.19 shows the percentage of time taken to import data,

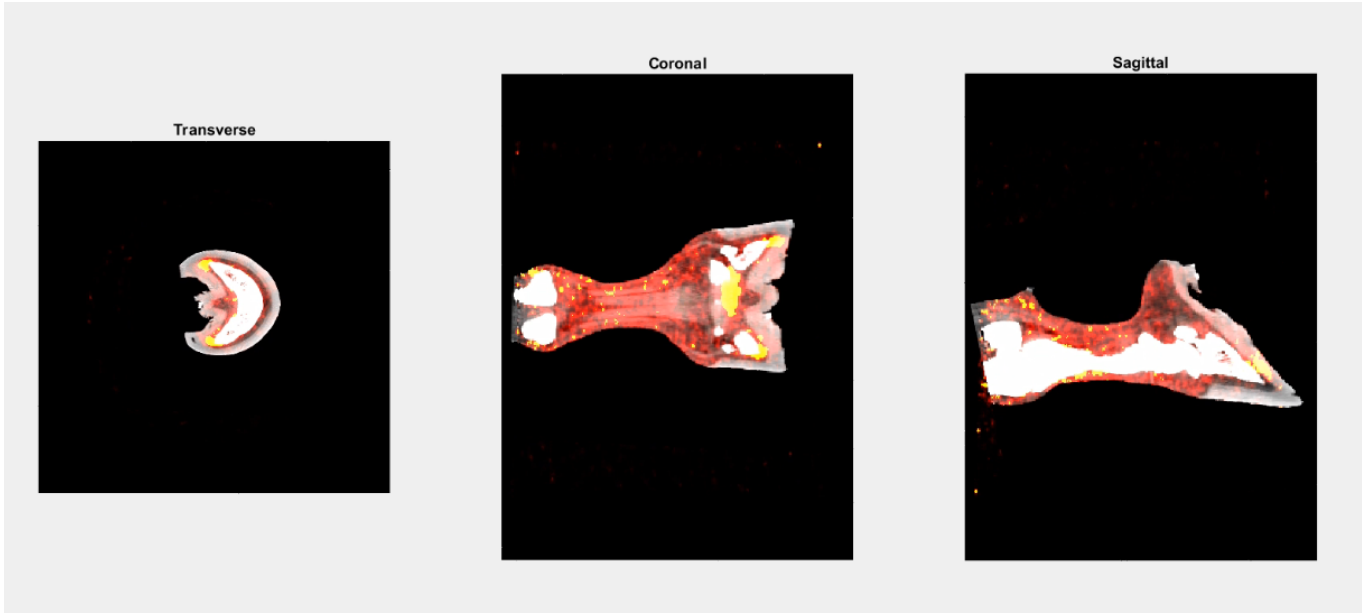


Figure 4.16: Registered 3D PET-CT shown as three 2D Images

pre-process and do coarse registration.

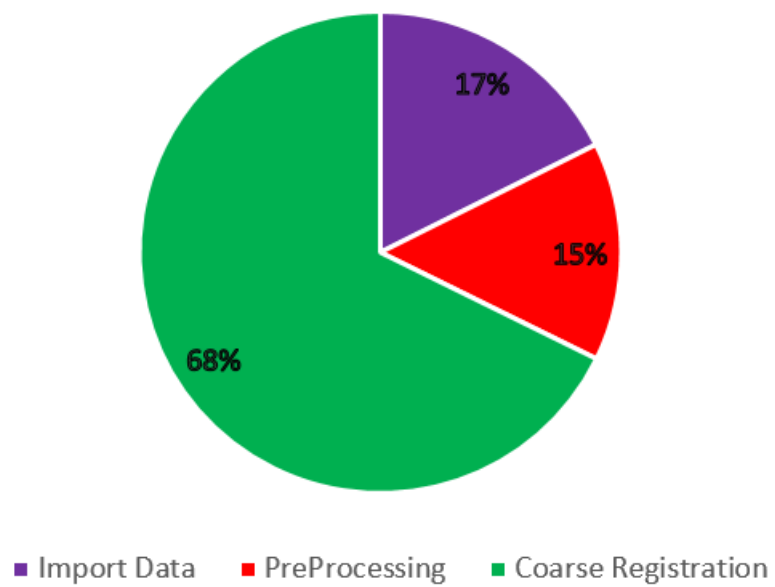


Figure 4.17: Percentage of time taken for each step in coarse registration

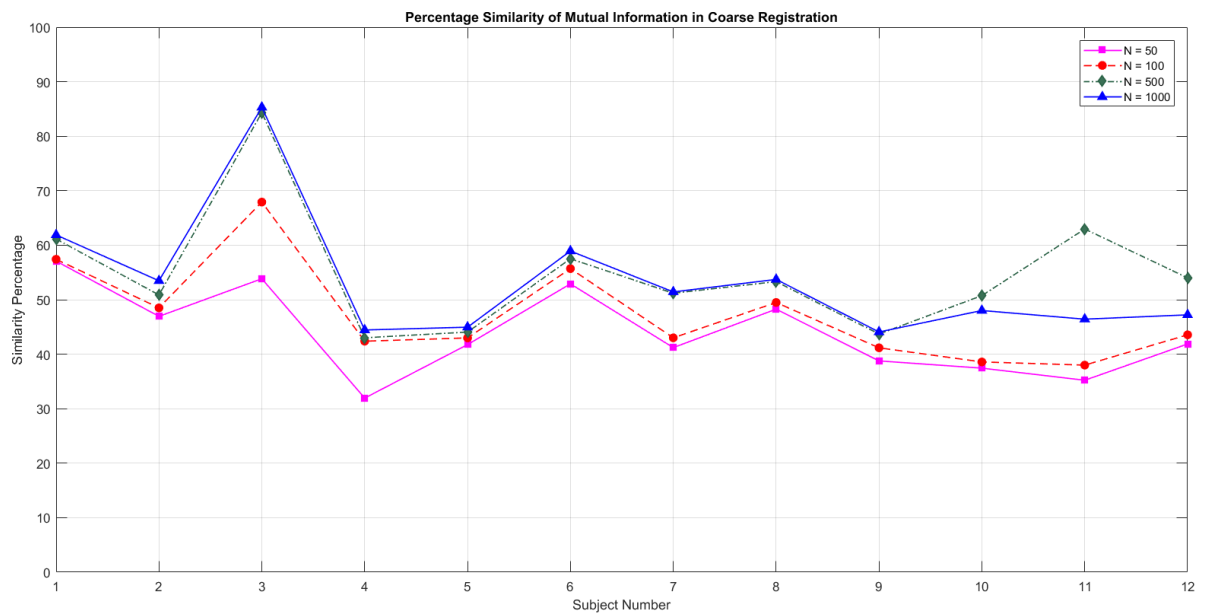


Figure 4.18: Mutual Information similarity percentage in the registration of PET-CT (N is the number of Iterations)

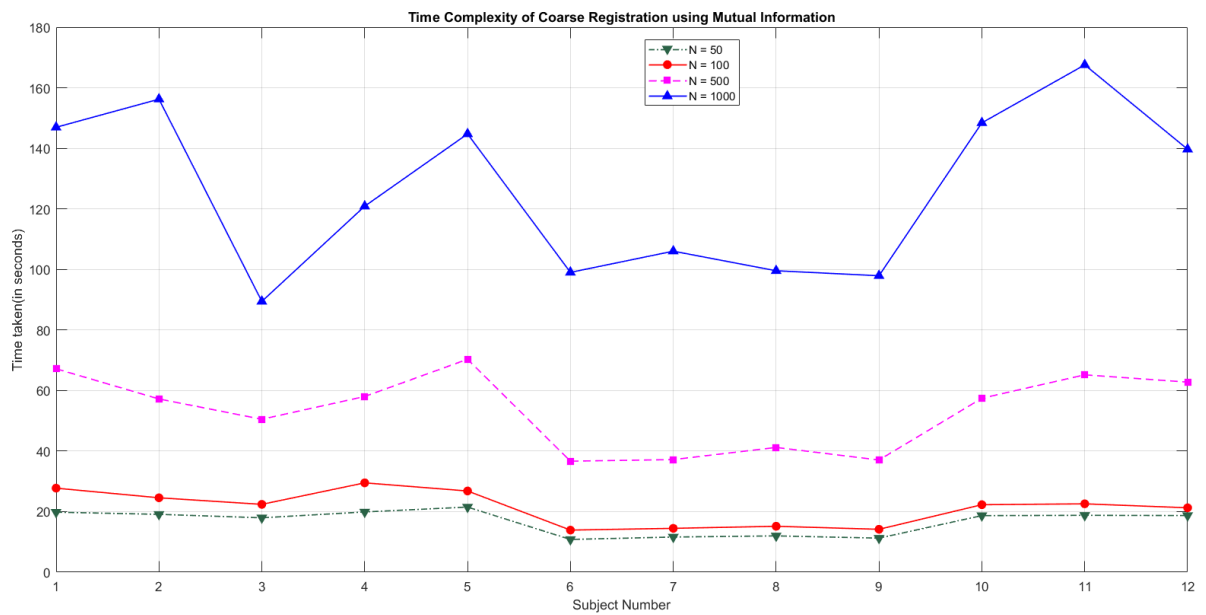


Figure 4.19: Time Complexity for Registration of PET-CT (N is the number of Iterations)

## Chapter 5: Automatic equine PET and CT image registration

Even in "automatic" image registration, we will have user interaction to some extent. Fig. 5.4 shows the different steps in the PET and CT registration process. We will discuss the details of these steps in this chapter.

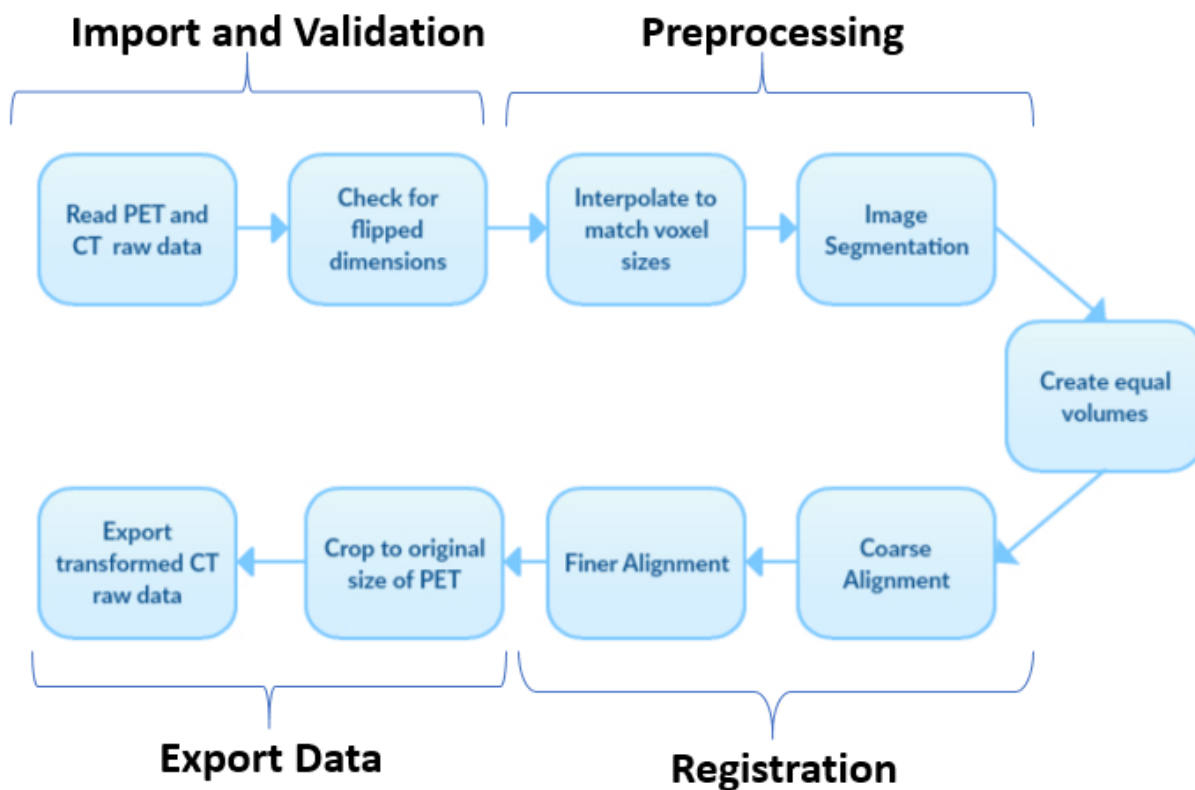


Figure 5.1: Different steps in the PET and CT registration.

The main stages in the registration process are:

- I Data import and validation
- II Preprocessing
- III Create equal volumes
- IV Registration
- V Export data

I Data import and validation

- (i) Read PET and CT raw data

To achieve compatibility between imaging systems present world wide, the Digital Imaging and Communications in Medicine (DICOM) standard is created. Fig. 5.2 shows a sample DICOM header which is followed by the raw data. Consider a three dimensional array with dimensions as *Height*, *Width* and *Depth*. Let  $x$ ,  $y$  and  $z$  be the corresponding indices. The three dimensional matrix  $threeDim(\textit{Height}, \textit{Width}, \textit{Depth})$  can be converted to a one-dimensional matrix  $oneDim(\textit{Height}, \textit{Width}, \textit{Depth})$  using the relation below:

$$oneDim[x + \textit{Height} \times (y - 1 + \textit{Width} \times (z - 1))] = threeDim[x, y, z] \quad (5.1)$$

- (ii) Check for flipped dimensions

```
      FileSize: 99617302
      Format: 'DICOM'
      FormatVersion: 3
      Width: 512
      Height: 512
      BitDepth: 16
      ColorType: 'grayscale'
FileMetaInformationGroupLength: 196
  FileMetaInformationVersion: [2x1 uint8]
  MediaStorageSOPClassUID: '1.2.840.10008.5.1.4.1.1.20'
  MediaStorageSOPInstanceUID: '777.777.0.0.0.1470278332.982387864.497233982.3985431486'
  TransferSyntaxUID: '1.2.840.10008.1.2.1'
  ImplementationClassUID: '0.0.0.0'
  ImplementationVersionName: 'NOTSPECIFIED'
  SourceApplicationEntityTitle: 'NOTSPECIFIED'
    ImageType: 'DERIVED\PRIMARY\RECON TOMO\EMISSION'
  InstanceCreationDate: '20160803'
  InstanceCreationTime: '223852'
  InstanceCreatorUID: '777.777.0.0.0'
    SOPClassUID: '1.2.840.10008.5.1.4.1.1.20'
  SOPInstanceUID: '777.777.0.0.0.1470278332.982387864.497233982.3985431486'
  StudyDate: ''
  SeriesDate: ''
  AcquisitionDate: ''
  ContentDate: ''
  StudyTime: '000000'
  SeriesTime: '000000'
```

Figure 5.2: Sample DICOM header

One of the steps in validation, before preprocessing, is to check for flipped dimensions before actual alignment. This can be done by visual inspection. One challenge with the equine scans is that the coronal section appears symmetric as shown in Fig. 5.3, it requires an experienced professional to figure out the orientation.

## II Preprocessing

- (i) Interpolate to match voxel sizes: The voxel in different modalities could be different and hence we need to interpolate before trying to apply any registration algorithms. The CT and PET voxels are shown in Fig. 5.4
- (ii) Image Segmentation: We have dealt with the image segmentation problem

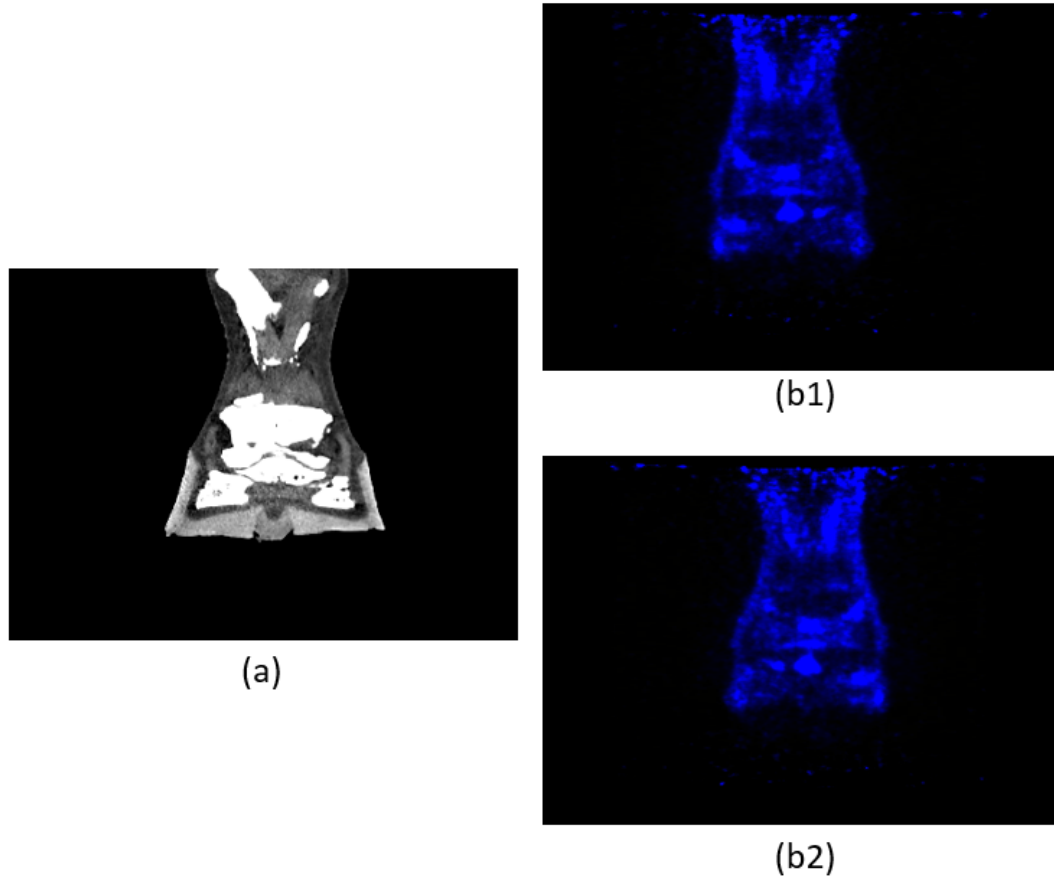


Figure 5.3: (a) shows a CT section, (b1) and (b2) show the corresponding PET section flipped with respect to each other. Observe that it is difficult to judge the correct alignment.

in detail in chapter 3. The regions to be segmented in CT before registering with PET also depend on the age of the horse. While the young horses require segmenting only the hoof part, the adult horses need to have the bones to be segmented along with the hoof region.

III Create equal volumes: We append zeros to match the two volumes so that we do not lose any information.

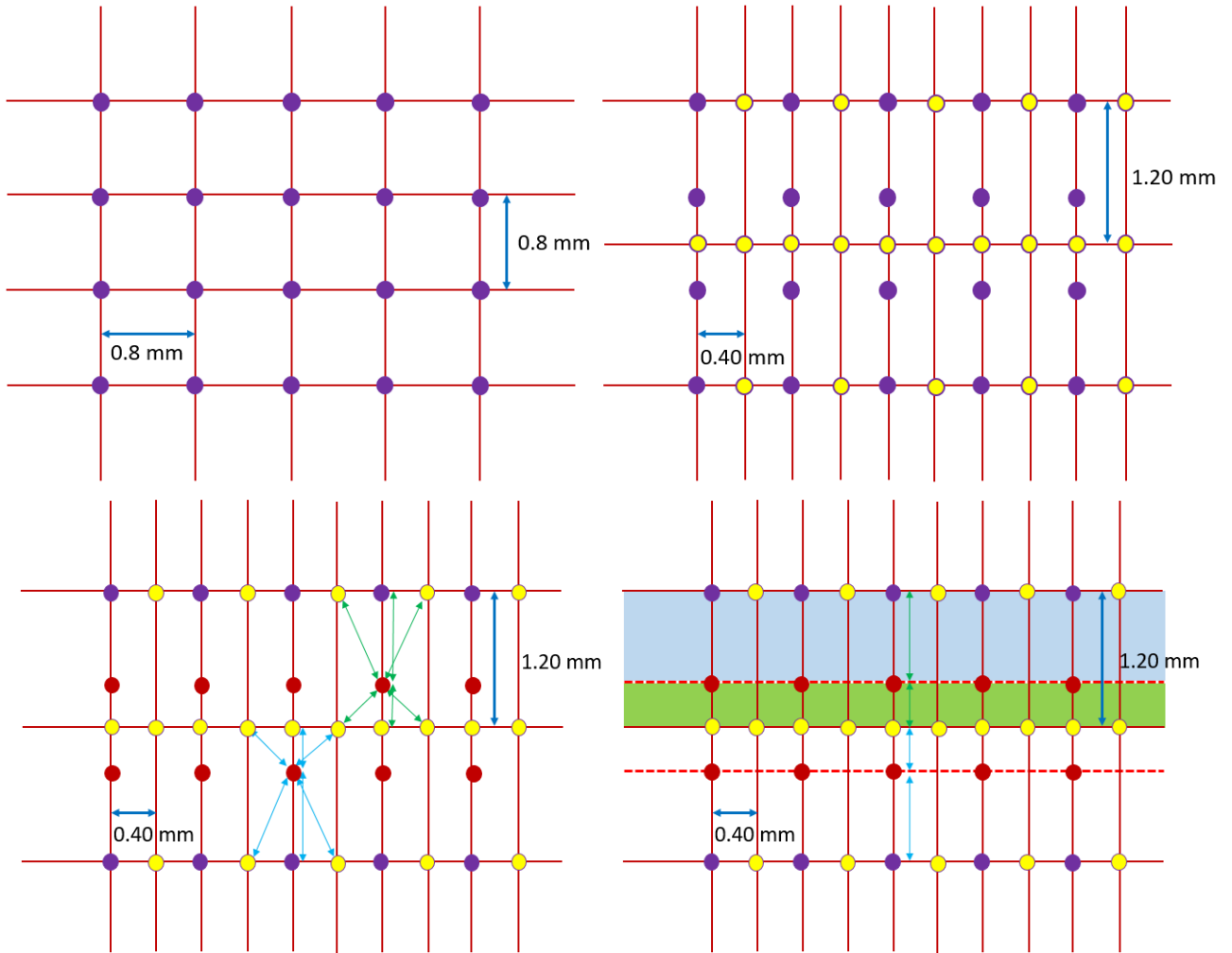


Figure 5.4: The PET and CT voxels: Interpolation

#### IV Registration

- (i) Coarse registration: Before using the algorithms for registration, a good initial condition is provided by the coarse registration. This is achieved by matching the center of intensities of the two images. Center of intensity is calculated similar to the center of mass of an object. The difference between the centers correspond to the translational parameters in the

coarse registration.

$$C_x = \frac{\sum_{i=1}^N I_i x_i}{\sum_{i=1}^N I_i} \quad (5.2)$$

$$C_y = \frac{\sum_{i=1}^N I_i y_i}{\sum_{i=1}^N I_i} \quad (5.3)$$

$$C_z = \frac{\sum_{i=1}^N I_i z_i}{\sum_{i=1}^N I_i} \quad (5.4)$$

Here N is the total number of voxels in the image.

- (ii) Fine registration: Some algorithms for registration have been discussed in chapter 4. The result of coarse registration is used as an initial condition for fine registration.

## V Export data

- (i) Crop to original size of PET : After registration, since we have used the PET image as the reference, the aligned CT image would also be in the same coordinates as of PET and hence we can crop it to the original dimensions of the PET image.
- (ii) Export transformed CT raw data: The three- dimensional array can be converted to one-dimensional array using the Eq. 5.1 and saved as a DICOM file.

## Chapter 6: Conclusions and Future Work

In the recent past, a new modality for horses, the PET imaging has been developed. Analysis showed that the PET images have information which is not present in other modalities like CT and MRI. Access to the functional and structural information in the same spatial coordinates enables us to identify and diagnose different lesions in horses. We considered the problem of registering PET and CT images in horses and tried to automate the process. We have described the different steps in detail and implemented a graphical user interface for the same. The next steps would be to optimize the algorithm and different stages of registration and reduce the time complexity from several minutes to a few seconds. Since the equine PET and CT registration problem does not possess infinite degrees of freedom, we can model the bone rotation and deal with deformable registration with two angles as two additional parameters. Image processing and machine learning techniques can be used to automatically announce the type of lesion present while reading the PET and CT images.

## Appendix A: The 3D PET-CT Image Registration GUI

We have developed an interactive graphical user interface in Qt(C++) to register 3D PET and CT images of horses. This implements automatic cropping, segmentation and registration modules with a provision to take the user inputs and modify, if necessary. This is being tested on new data sets and once proved to be robust enough can get rid of many debugging options and made accessible to the general audience.

Fig. [A.1](#) shows the axes using which the 3D image is displayed as a combination of three 2D images. The scroll bar adjacent to the 2D images can be used to traverse different slices of the images in the respective axes. Fig. [A.2](#) highlights some options in the GUI and Fig. [A.3](#) shows the MIP (Maximum Intensity Projection) Images.

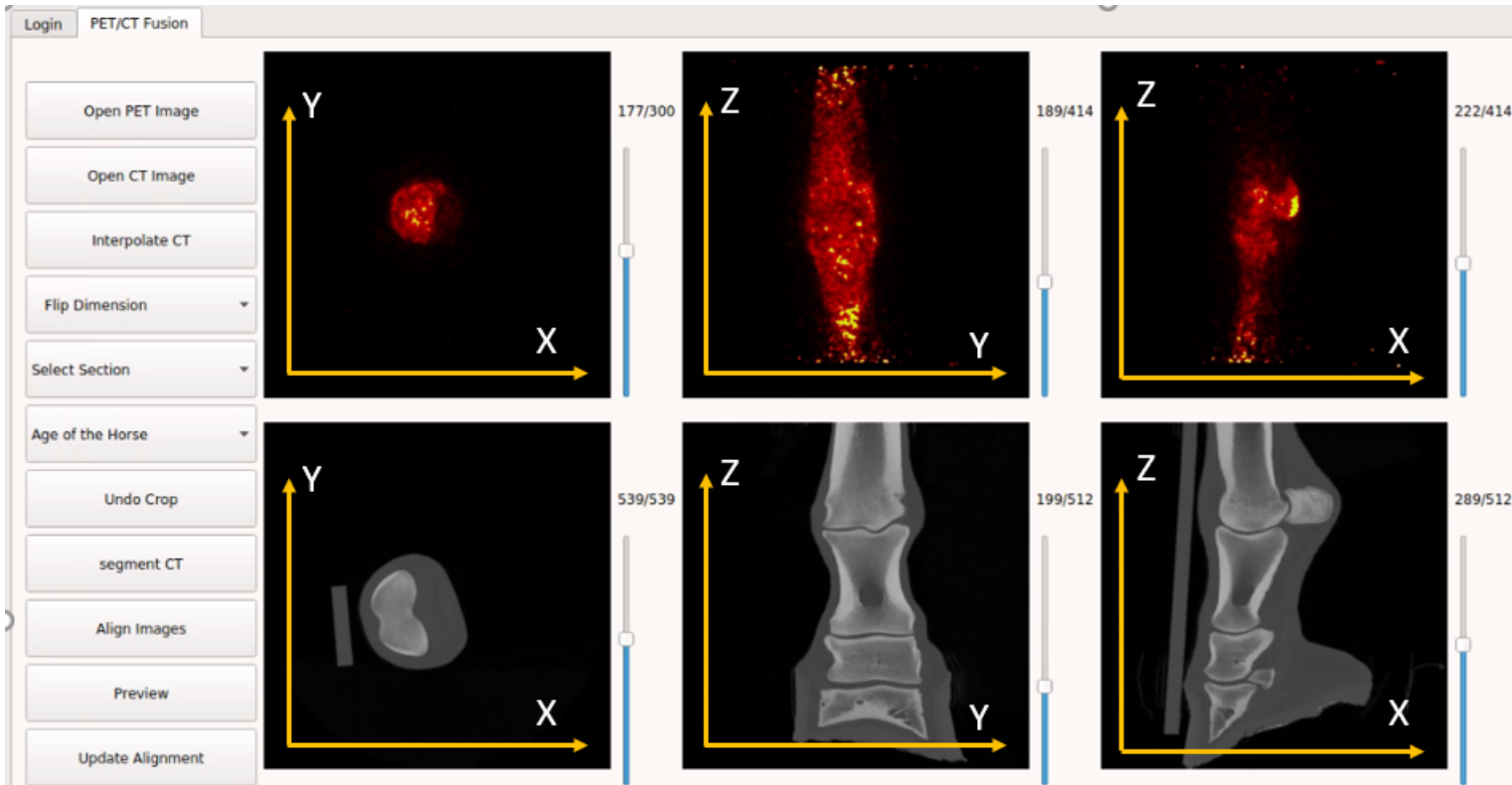


Figure A.1: Axes in GUI

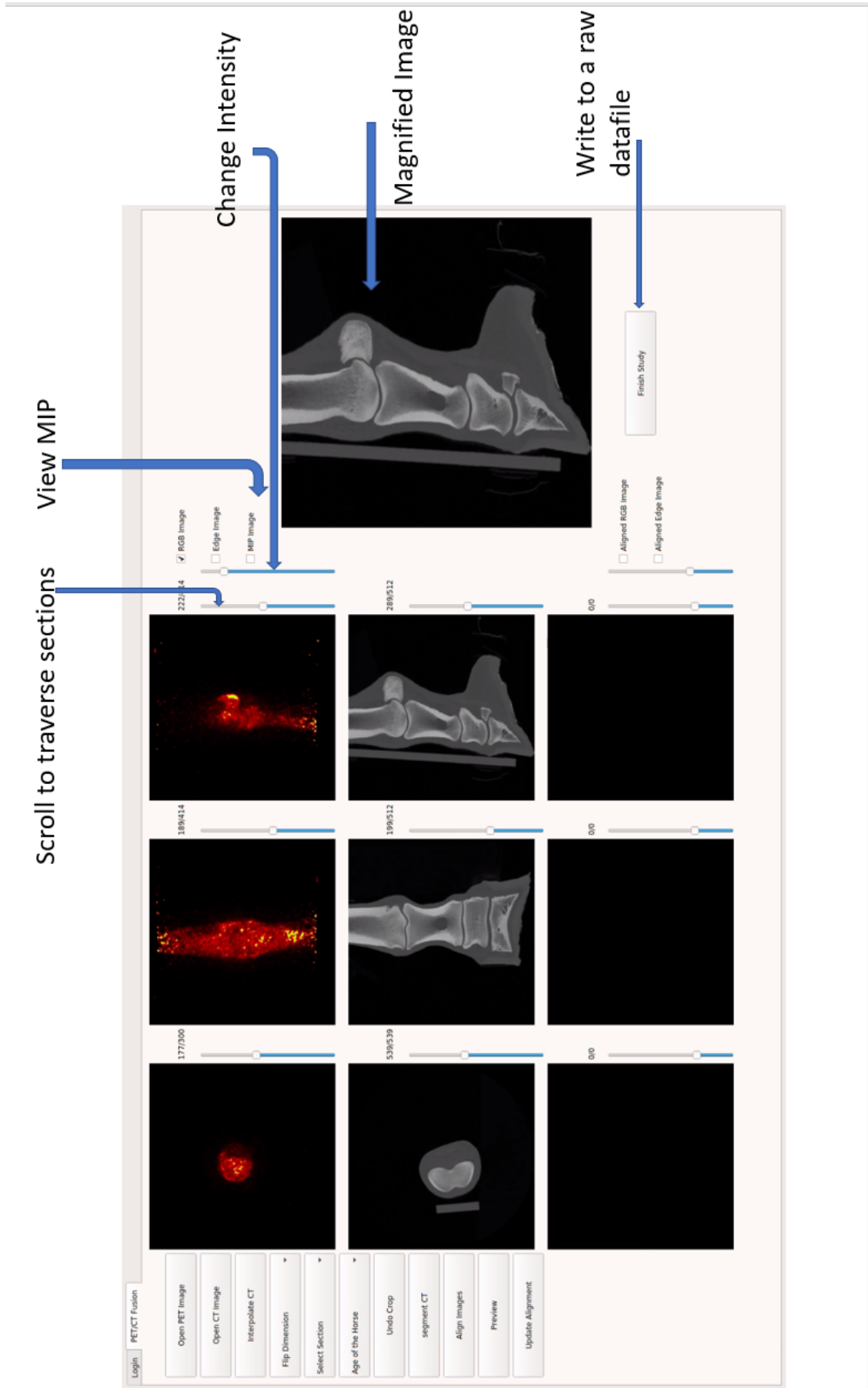


Figure A.2: Modules in the PET-CT GUI

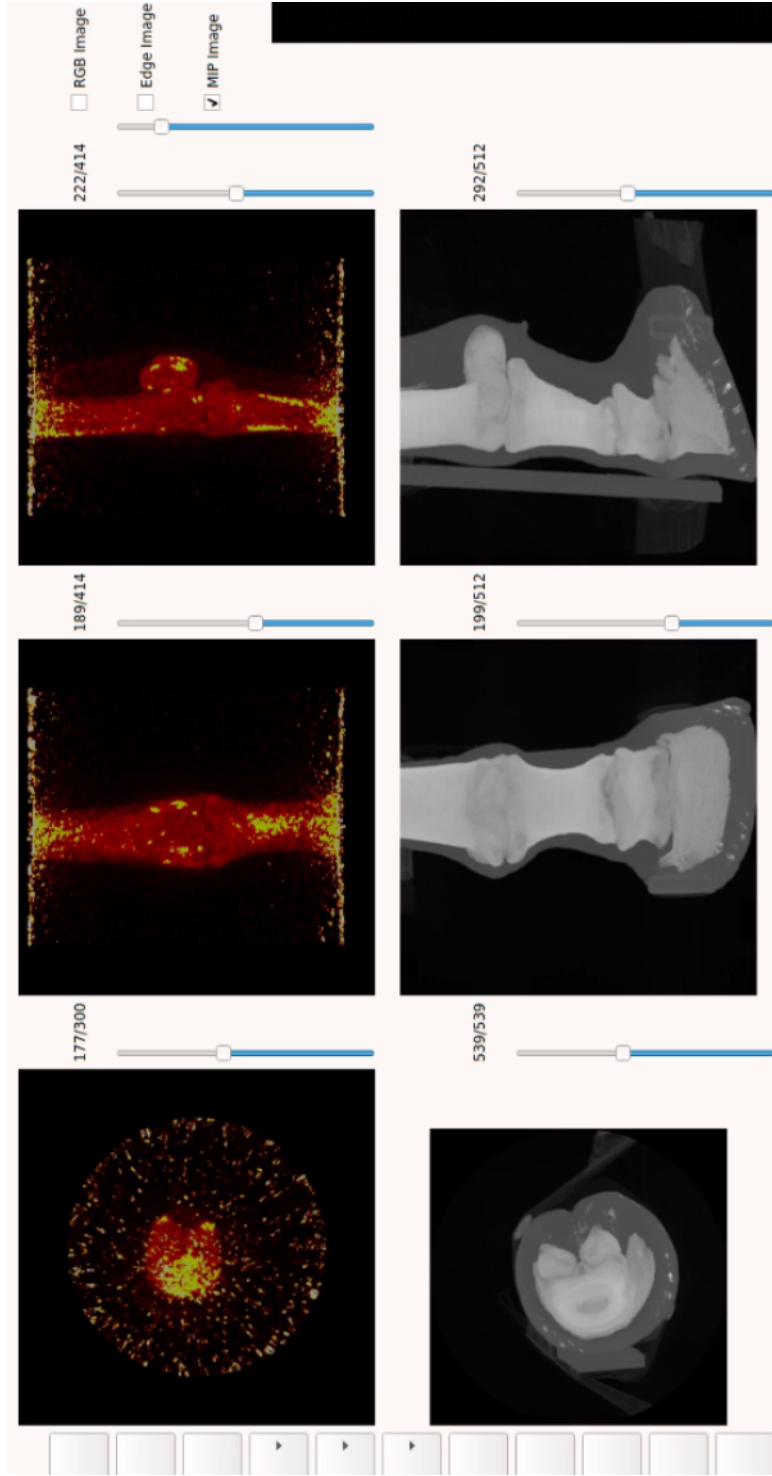


Figure A.3: MIP Images of PET and CT in GUI

## Bibliography

- [1] Segmentation in Medical Imaging.
- [2] C Arl and D Anderson. The production and properties of positrons.
- [3] Yuri Boykov and Vladimir Kolmogorov. An Experimental Comparison of Min-Cut/Max-Flow Algorithms for Energy Minimization in Vision.
- [4] Yuri Y Boykov and Marie-Pierre Jolly. Interactive Graph Cuts for Optimal Boundary & Region Segmentation of Objects in N-D Images. 2001.
- [5] P A Bromiley and N A Thacker. Multi-dimensional Medical Image Segmentation with Partial Volume and Gradient Modelling Supplement 1: Mathematical Derivations and Proofs. *Annals of the BMVA*, (2s1):1–11, 2008.
- [6] H. M. Clayton, D. H. Sha, and D. R. Mullineaux. Three-dimensional Torques and Power of Horse Forelimb Joints at Trot. aug 2011.
- [7] Jian S. Dai. EulerRodrigues formula variations, quaternion conjugation and intrinsic connections. *Mechanism and Machine Theory*, 92:144–152, 2015.
- [8] Lee R. Dice. Measures of the Amount of Ecologic Association Between Species. *Ecology*, 26(3):297–302, jul 1945.
- [9] Richard O Duda Peter E Hart David G Stork and New York Chichester Weinheim Brisbane Singapore Toronto. PATTERN CLASSIFICATION Second Edition.
- [10] Frederic H Fahey Dsc. What You Should Know About Radiation and Nuclear Medicine.
- [11] Amanda Gaudreau-Balderrama. MULTI-MODAL IMAGE REGISTRATION. 2012.

- [12] Stuart Geman and Donald Geman. Stochastic relaxation, Gibbs distributions and the Bayesian restoration of images\*. *Journal of Applied Statistics*, 20(5-6):25–62, jan 1993.
- [13] E.R. Hancock and J. Kittler. Edge-labeling using dictionary-based relaxation. *IEEE Transactions on Pattern Analysis and Machine Intelligence*, 12(2):165–181, 1990.
- [14] Jonathan Hearn. COMPETITIVE MEDICAL IMAGE SEGMENTATION WITH THE FAST MARCHING METHOD. 2008.
- [15] Berthold K P Horn, Hugh M Hilden, Shahriar Negahdaripour, B K P Horn, H M Hilden, and S Negahdaripour. Closed-Form Solution of Absolute Orientation Using Orthonormal Matrices. Closed-Form Solution of Absolute Orientation Using Orthonormal Matrices.
- [16] HL Huang, HD Lin, BT Chung, and KP Lin. Structural and functional image registration using maximum mutual information. *Journal of Medical and*, 2003.
- [17] Hassana Grema Kaganami and Zou Bei. Region-Based Segmentation versus Edge Detection. In *2009 Fifth International Conference on Intelligent Information Hiding and Multimedia Signal Processing*, pages 1217–1221. IEEE, sep 2009.
- [18] Heikki Kälviäinen, Petri Hirvonen, Lei Xu, and Erkki Oja. Probabilistic and non-probabilistic Hough transforms: overview and comparisons. *Image and Vision Computing*, 13(4):239–252, may 1995.
- [19] T. Law, H. Itoh, and H. Seki. Image filtering, edge detection, and edge tracing using fuzzy reasoning. *IEEE Transactions on Pattern Analysis and Machine Intelligence*, 18(5):481–491, may 1996.
- [20] Yuh-Tay Liow. A contour tracing algorithm that preserves common boundaries between regions. *CVGIP: Image Understanding*, 53(3):313–321, may 1991.
- [21] Graeme Mason, Martin Bendszus, Dieter Meyerhoff, Hoby Hetherington, Brian Schweinsburg, Brian Ross, Michael Taylor, and John Krystal. Magnetic resonance spectroscopic studies of alcoholism: from heavy drinking to alcohol dependence and back again. *Alcoholism, clinical and experimental research*, 29(1):150–158, jan 2005.
- [22] David Mattes, David R Haynor, Hubert Vesselle, Thomas K Lewellen, and William Eubank. PET-CT Image Registration in the Chest Using Free-form Deformations. *IEEE TRANSACTIONS ON MEDICAL IMAGING*, 22(1), 2003.
- [23] Thomas Netsch, Peter Roesch, Juergen Weese, Arianne van Muiswinkel, and Paul Desmedt. Grey-value-based 3D registration of functional MRI time-series: comparison of interpolation order and similarity measure. pages 1148–1159. International Society for Optics and Photonics, jun 2000.

- [24] Alireza Norouzi, Mohd Shafry Mohd Rahim, Ayman Altameem, Tanzila Saba, Abdolvahab Ehsani Rad, Amjad Rehman, and Mueen Uddin. Medical Image Segmentation Methods, Algorithms, and Applications. *IETE Technical Review*, 31(3):199–213, may 2014.
- [25] Tamar Peli and David Malah. A study of edge detection algorithms. *Computer Graphics and Image Processing*, 20(1):1–21, sep 1982.
- [26] Dzung L. Pham, Chenyang Xu, and Jerry L. Prince. Current Methods in Medical Image Segmentation. *Annual Review of Biomedical Engineering*, 2(1):315–337, aug 2000.
- [27] Y. Picard and C.J. Thompson. Motion correction of PET images using multiple acquisition frames. *IEEE Transactions on Medical Imaging*, 16(2):137–144, apr 1997.
- [28] Neeraj Sharma and Lalit M Aggarwal. Automated medical image segmentation techniques. *Journal of medical physics*, 35(1):3–14, jan 2010.
- [29] Kritika Sharma Mtech Student. Restoration of Medical Images using Blind Image Deconvolution based on Ant Colony Sheetal Kundra. *International Journal of Computer Applications*, 84(16):975–8887, 2013.
- [30] Lazy Snapping, Yin Li, Jian Sun, Chi-Keung Tang, Heung-Yeung Shum, and Hong Kong. LazySnapping.
- [31] Mathieu Spriet, Pablo Espinosa, Andre Z. Kyme, Pavel Stepanov, Val Zavarzin, Stephen Schaeffer, Scott A. Katzman, Larry D. Galuppo, and David Beylin. POSITRON EMISSION TOMOGRAPHY OF THE EQUINE DISTAL LIMB: EXPLORATORY STUDY. *Veterinary Radiology & Ultrasound*, 57(6):630–638, nov 2016.
- [32] Martin Styner, Christian Brechbühler, Gábor Székely, and Guido Gerig. Parametric estimate of intensity inhomogeneities applied to MRI. *IEEE TRANSACTIONS ON MEDICAL IMAGING*, 19(3):153–165, 2000.
- [33] Michel M. Ter-Pogossian. Positron Emission Tomography (PET). In *Diagnostic Imaging in Medicine*, pages 273–277. Springer Netherlands, Dordrecht, 1983.
- [34] Jussi Tohka. Partial volume effect modeling for segmentation and tissue classification of brain magnetic resonance images: A review. *World journal of radiology*, 6(11):855–64, nov 2014.
- [35] S. Umeyama. Least-squares estimation of transformation parameters between two point patterns. *IEEE Transactions on Pattern Analysis and Machine Intelligence*, 13(4):376–380, apr 1991.

- [36] Luc Vincent and Pierre Soille. Watersheds in Digital Spaces: An Efficient Algorithm Based on Immersion Simulations. *IEEE TRANSACTIONS ON PATTERN ANALYSIS AND MACHINE INTELLIGENCE*, 13(6), 1991.
- [37] Uroš Vovk, Franjo Pernuš, and Boštjan Likar. A Review of Methods for Correction of Intensity Inhomogeneity in MRI. *IEEE TRANSACTIONS ON MEDICAL IMAGING*, 26(3), 2007.
- [38] Xiang Li, D. Eremina, Lihong Li, and Zhengrong Liang. Partial volume segmentation of medical images. In *2003 IEEE Nuclear Science Symposium. Conference Record (IEEE Cat. No.03CH37515)*, pages 3176–3180. IEEE.
- [39] Hui Zhang, Jason E Fritts, and Sally A Goldman. Image segmentation evaluation: A survey of unsupervised methods. 2007.